Article

Cell Reports

Single-Cell Transcriptomics Characterizes Cell Types in the Subventricular Zone and Uncovers Molecular Defects Impairing Adult Neurogenesis

Graphical Abstract

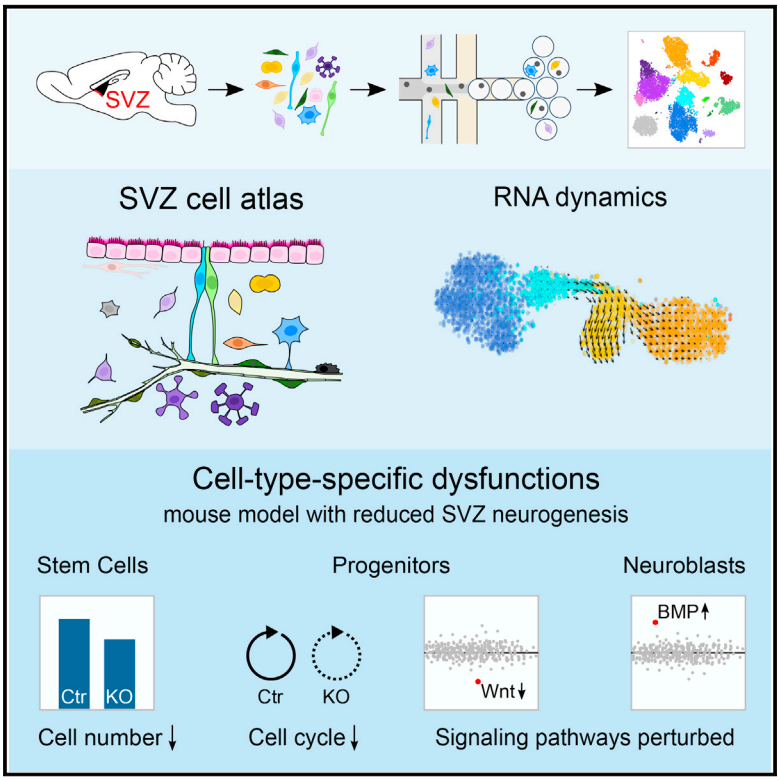

Authors

Vera Zywitza, Aristotelis Misios, Lena Bunatyan, Thomas E. Willnow, Nikolaus Rajewsky

Correspondence

willnow@mdc-berlin.de (T.E.W.), rajewsky@mdc-berlin.de (N.R.)

In Brief

Zywitza et al. use single-cell transcriptomics to establish a comprehensive cell atlas of the largest germinal region in the adult mouse brain, the subventricular zone (SVZ). They demonstrate the applicability of this atlas to elucidate cell-type-specific changes underlying impaired neurogenesis in mouse models.

Highlights

- Single-cell transcriptomics characterizes the SVZ adult neural stem cell niche
- Free online tool to assess gene expression across 9,804 single cells
- Different transcriptional dynamics along the neurogenic lineage
- Cell-type-specific dysfunctions underlying impaired adult neurogenesis

Zywitza et al., 2018, Cell Reports *25*, 2457–2469
November 27, 2018 © 2018 The Author(s).
https://doi.org/10.1016/j.celrep.2018.11.003

CellPress

Cell Reports
Article

OPEN ACCESS
CellPress

Single-Cell Transcriptomics Characterizes Cell Types in the Subventricular Zone and Uncovers Molecular Defects Impairing Adult Neurogenesis

Vera Zywitza,[1,3] Aristotelis Misios,[1,3] Lena Bunatyan,[2] Thomas E. Willnow,[2,*] and Nikolaus Rajewsky[1,4,*]
[1]Systems Biology of Gene Regulatory Elements, Berlin Institute for Medical Systems Biology, Max Delbrück Center for Molecular Medicine in the Helmholtz Association, 13092 Berlin-Buch, Germany
[2]Molecular Cardiovascular Research, Max Delbrück Center for Molecular Medicine in the Helmholtz Association, 13092 Berlin-Buch, Germany
[3]These authors contributed equally
[4]Lead Contact
*Correspondence: willnow@mdc-berlin.de (T.E.W.), rajewsky@mdc-berlin.de (N.R.)
https://doi.org/10.1016/j.celrep.2018.11.003

SUMMARY

Neural stem cells (NSCs) contribute to plasticity and repair of the adult brain. Niches harboring NSCs regulate stem cell self-renewal and differentiation. We used comprehensive and untargeted single-cell RNA profiling to generate a molecular cell atlas of the largest germinal region of the adult mouse brain, the subventricular zone (SVZ). We characterized >20 neural and non-neural cell types and gained insights into the dynamics of neurogenesis by predicting future cell states based on computational analysis of RNA kinetics. Furthermore, we applied our single-cell approach to document decreased numbers of NSCs, reduced proliferation activity of progenitors, and perturbations in Wnt and BMP signaling pathways in mice lacking LRP2, an endocytic receptor required for SVZ maintenance. Our data provide a valuable resource to study adult neurogenesis and a proof of principle for the power of single-cell RNA sequencing to elucidate neural cell-type-specific alterations in loss-of-function models.

INTRODUCTION

Adult neurogenesis is important for the cellular plasticity of the brain. In the adult mammalian brain, the generation of new neurons is restricted to two major sites: the subventricular zone (SVZ) of the lateral ventricles and the subgranular zone (SGZ) in the dentate gyrus (DG) of the hippocampus. In the adult SVZ, radial-glia-like cells serve as neural stem cells (NSCs) and give rise to transient amplifying progenitors (TAPs), which in turn generate neuroblasts (NBs). NBs migrate along the rostral migratory stream toward the olfactory bulb, where they terminally differentiate into specific subtypes of interneurons and integrate into existing neural circuits (reviewed in Ming and Song, 2011) (Figure 1, left).

Adult NSCs reside in a specialized niche, where they are in immediate contact with various cell types. Cell-intrinsic factors and the microenvironment provided by the niche are both crucial for balancing stem cell self-renewal, proliferation, and differentiation (reviewed in Bjornsson et al., 2015). Understanding the potential of single NSCs and the underlying principles of NSC regulation is necessary for potentially using these cells as an endogenous source for treating brain injuries or neurodegenerative diseases.

To characterize the entire SVZ neurogenic niche at the single-cell level in an untargeted and comprehensive manner, we used Drop-seq, a microfluidic- and nanodroplet-based highly parallel transcriptome profiling technology (Macosko et al., 2015). In contrast to previous single-cell RNA sequencing studies, which isolated NSCs and a few selected cell types based on the expression of marker genes (i.e., Basak et al., 2018; Dulken et al., 2017; Llorens-Bobadilla et al., 2015; Luo et al., 2015; Shah et al., 2018; Shin et al., 2015), our strategy circumvents preselection. Thus, we include all SVZ-residing cells and minimize the risks of missing potentially undescribed or marker-negative cell populations. We identified more than 20 neural and non-neural cell types residing in the SVZ and provided their gene expression signatures. Sequencing data are readily accessible via a public online tool that allows investigators to evaluate and visualize the expression of their genes of interest in the context of 22 distinct cell types and 9,804 individual cells. We resolved NSC activation states and uncovered differences in RNA dynamics in NSCs and their progeny by estimating future cell states using a model for mRNA maturation, which is based on calculating the ratios of measured unspliced (premature mRNAs) and spliced (mature mRNAs) sequencing reads (La Manno et al., 2018).

We used the untargeted single-cell transcriptome profiling approach to investigate cell-type-specific molecular changes in the SVZ of mice mutant for low-density lipoprotein receptor-related protein 2 (LRP2, also known as megalin). LRP2 is a multifunctional endocytic receptor expressed in multiple tissues, including the SVZ of the adult brain. LRP2 activity is indispensable for proper development and function of various tissues, including forebrain, eye, and heart (reviewed in Christ et al., 2016). In humans, mutations in *Lrp2* are the cause of Donnai-Barrow syndrome (Kantarci et al., 2007), a severe autosomal

This is an open access article under the CC BY-NC-ND license (http://creativecommons.org/licenses/by-nc-nd/4.0/).

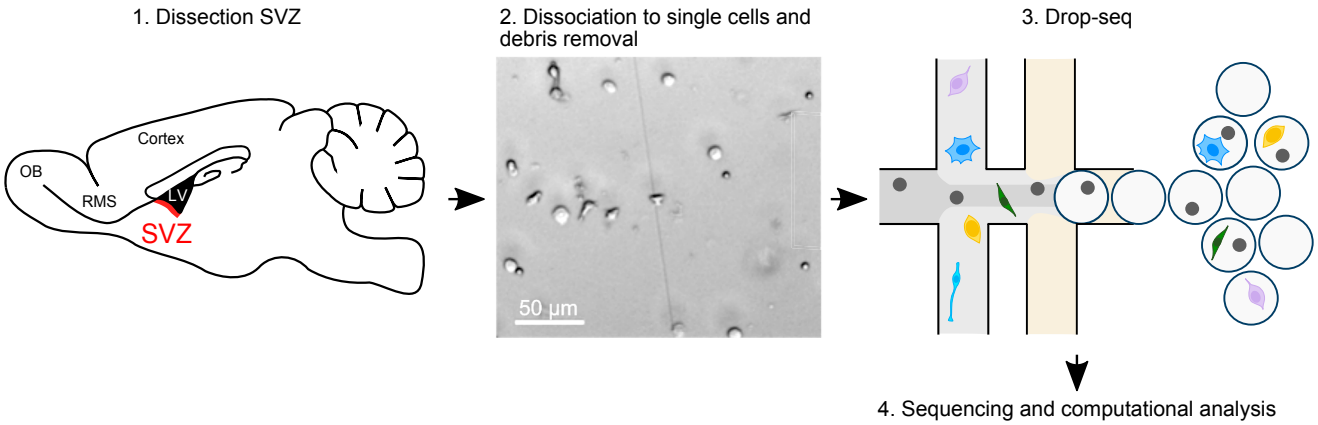

Figure 1. Single-Cell RNA Sequencing of the Adult SVZ

After microdissection of the subventricular zone (SVZ) (1, marked in red), the tissue was dissociated into single cells. Debris, dead cells, and cell clumps were removed. The single-cell suspension (2) was applied to a microfluidic device, in which single cells were combined with barcoded beads in droplets (3). After library preparation and sequencing, single-cell transcriptomes were deconvolved and analyzed (4). Left: sagittal section view of the adult mouse brain. SVZ, subventricular zone; OB, olfactory bulb; RMS, rostral migratory stream; LV, lateral ventricle.

recessive disorder affecting multiple organ systems. These abnormalities are recapitulated in LRP2-deficient mice (Willnow et al., 1996). With relevance to our study, LRP2 is expressed in the ependymal cell layer facing the SVZ neurogenic niche. Loss of LRP2 expression in gene-targeted mice results in impaired adult neurogenesis specifically in the SVZ, but not the SGZ (where the receptor is not expressed) (Gajera et al., 2010). To investigate which cell types in the SVZ are affected and how, we performed comparative single-cell RNA sequencing of SVZ tissues dissected from LRP2-deficient mice and matched littermate controls. We show that the number of NSCs and proliferating cells is reduced in mutant mice and that TAPs express fewer genes associated with cell-cycle control. Differential gene expression analysis per cell type revealed perturbations in bone morphogenetic protein (BMP) and Wnt signaling in NBs and TAPs, respectively, and a global reduction in ribosomal protein gene expression. We validated these single-cell RNA sequencing results by immunohistochemistry and propose a role for LRP2 in integrating the activity of several morphogen pathways in the SVZ to provide the appropriate microenvironment for functional neurogenesis to proceed.

Altogether, this study (1) demonstrates that our comprehensive single-cell RNA sequencing strategy enables an untargeted analysis of NSCs within the context of the entire neurogenic niche, (2) reveals consequences of LRP2 ablation on adult SVZ neurogenesis, and (3) provides a resource for studying adult neurogenesis.

RESULTS

The Entire Adult SVZ Neurogenic Niche at Single-Cell Resolution

To study adult NSCs, their progeny, and surrounding niche cells as comprehensively and unbiasedly as possible, we microdissected the SVZs from three to five mice and generated a high-quality single-cell suspension using an optimized tissue dissociation and debris removal protocol (see STAR Methods for details). We then performed Drop-seq (Macosko et al., 2015), a droplet-based single-cell transcriptome profiling method, to simultaneously obtain the transcriptome of thousands of cells (Figure 1). Computational analysis of sequencing data was performed with Seurat v.1.4 (Satija et al., 2015). To reduce the dimension of data, the most highly variable genes were selected for principal component (PC) analysis. Subsequently, all PCs with a p value smaller than 0.01 were used for clustering with the shared nearest neighbor (SNN) algorithm and for data visualization with t-distributed stochastic neighbor embedding (tSNE) as implemented in Seurat.

We collected 9,804 cells with 734 genes and 1,137 unique molecular identifiers (UMIs) quantified per cell (medians) in five replicates (Figure S1A). Independent analysis of replicates revealed similar results (data not shown). Gene expression levels from live and methanol-fixed cells correlated well (Figure S1B). To gain higher resolution, we jointly analyzed cells from all replicates. We did not observe batch effects, because cell clusters contained cells from all replicates in similar proportions (Figures S1C and S1D). Initial analysis identified 17 distinct cell clusters (Figure 2A), which could be assigned to known cell types based on the detection of known marker genes (Figures 2B and S2). Cell-type-enriched genes were identified by comparing each cluster to all others (Table S1). Exemplarily, we show the expression of the top five genes from each cell cluster across all cells (Figure 2C).

Characterization of Cell Types Residing in the Adult SVZ

NSCs formed a cluster in the center of the tSNE plot (Figure 2A). We identified them based on (1) their similarity to astrocytes (Doetsch et al., 1999); (2) the expression of *Thbs4*, which was previously reported to be highly enriched in NSCs (Beckervordersandforth et al., 2010; Llorens-Bobadilla et al., 2015); and (3) upregulation of genes associated with NSC activation, such as *Ascl1* at the upper part of the cluster (Figure 2D, blue

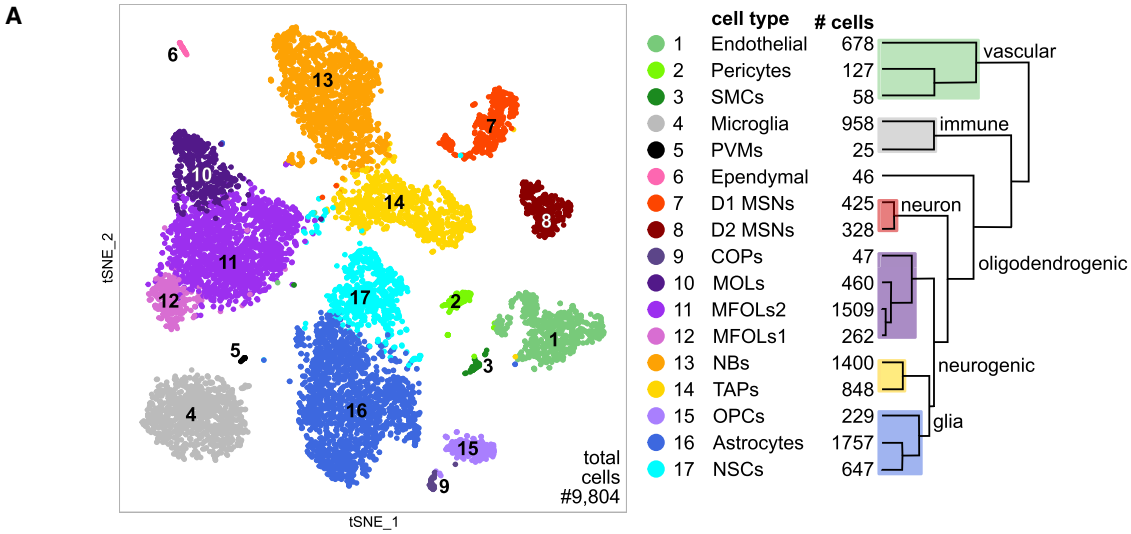

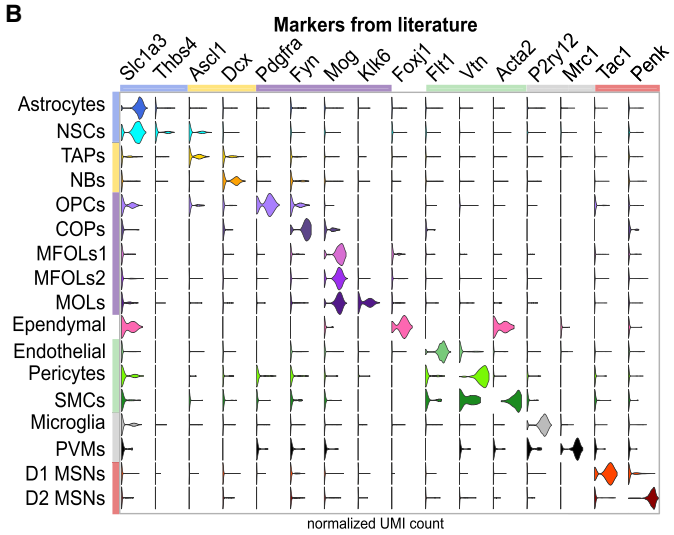

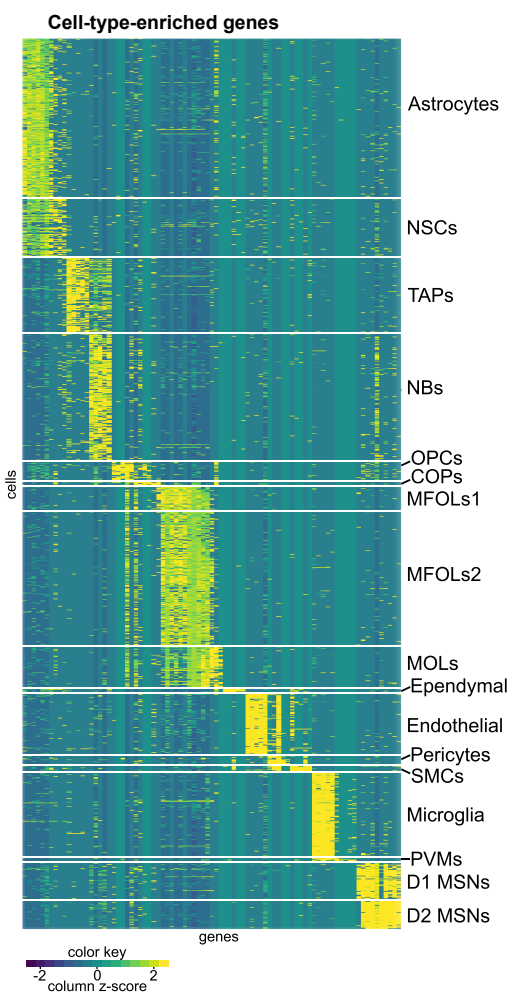

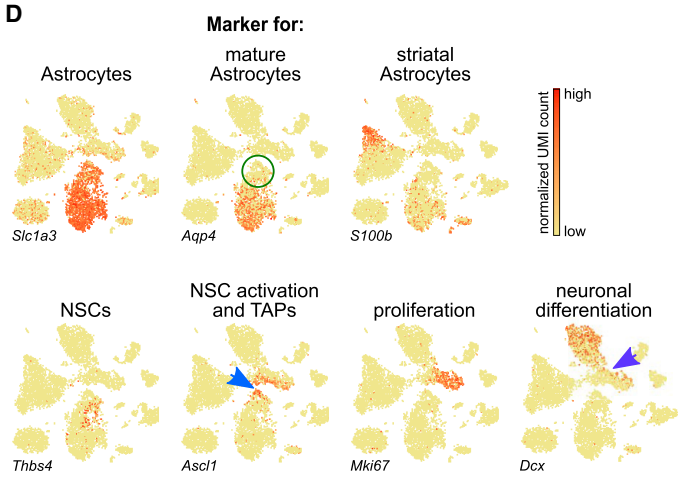

(legend on next page)

arrow). The commonly used stem cell markers *Nes* and *Prom1* (CD133 in human) (reviewed in Chaker et al., 2016) were rarely expressed in NSCs but were mostly detected in endothelial cells (Figure S3, see below). NSCs shared the expression profile with astrocytes. For example, *Slc1a3* (*Glast*) was highly enriched in both cell types. By contrast, NSCs and most astrocytes were negative for *S100b* (here, mainly detected in mature oligodendrocytes [MOLs] and ependymal cells) (Figure 2D), which is a marker for astrocytes residing deeper in the tissue at the interface to the striatum (Codega et al., 2014). These findings strongly suggest that clusters 17 and 16 of our dataset consist of NSCs and niche astrocytes, respectively. Despite overlapping expression profiles, the breadth of our dataset enabled us to resolve NSCs from niche astrocytes and to identify significantly up- and downregulated genes (Table S2). In Figure 2D, we show exemplarily that *Aqp4*, a marker of mature astrocytes, is barely detected in NSCs (green circle). Previous single-cell RNA sequencing studies could not separate NSCs and niche astrocytes (Basak et al., 2018; Dulken et al., 2017).

Adjacent to NSCs, TAPs composed a cluster enriched for proliferation markers, such as *Mki67* and *Pcna*, and genes associated with neuronal commitment, such as *Dlx1* and *Dlx2* (Figures 2D and S2). We detected genes known to be involved in neuronal differentiation (e.g., *Dcx* and *Tubb3*) in TAPs, which are close to the NB cluster (Figure 2D, purple arrow). The expression of neuronal marker genes increased toward the tip of cluster 13 (NBs) (Figures 2D and S2).

Based on the expression of marker genes such as *Flt1*, we identified cells of cluster 1 as endothelial cells (Figures 2B and S3). As mentioned earlier, we observed that these cells express markers reported to be associated with other cell types. For example, PROM1 (CD133 in human), a microvilli and primary cilia-associated protein (Dubreuil et al., 2007; Weigmann et al., 1997), is widely used to identify and isolate ependymal cells and, in combination with GFAP or GLAST, NSCs (Beckervordersandforth et al., 2010; Fischer et al., 2011; Llorens-Bobadilla et al., 2015). At the RNA level, we detected *Prom1* to be co-expressed with known markers of endothelial cells (e.g., *Flt1* and *Slc2a1/Glut1*) (Figures S3A and S3B). In addition to *Prom1*, endothelial cells were positive for *Vim* and *Nes*, markers for ependymal and neural progenitor cells, respectively (Figures S3A and S3B). Conversely, the endothelial marker *Slc2a1* was co-expressed with the ependymal markers *Foxj1* and *Ak7* in cluster 6 (Figures S2, S3A, and S3B). Therefore, we conclude that endothelial and ependymal cells share the expression of some established marker genes. Evaluation of (1) *in situ* images of the Allen Brain Atlas (Lein et al., 2007) and (2) bulk RNA sequencing data from purified cell populations (Zhang et al., 2014) supported our findings (Figures S3C and S3D).

Furthermore, we identified two types of mural cells (pericytes and smooth muscle cells [SMCs]), two distinct clusters consisting of immune cells (microglia and perivascular macrophages [PVMs]), five clusters comprising different stages of the oligodendrocyte lineage (oligodendrocyte progenitor cells [OPCs], differentiation-committed oligodendrocyte precursors [COPs], myelin-forming oligodendrocytes [MFOLs1 and MFOLs2], and MOLs [Marques et al., 2016]), and two clusters of mature neurons (markers used for cell-type identification in Figures 2B and S2). OPCs clustered close to NSCs and astrocytes, indicating higher similarity of OPCs to astroglia than to oligodendroglia (Figure 2A, dendogram).

Based on the expression of marker genes like *Tac1* and *Pdyn* or *Penk* and *Adora2a*, it appears that the observed mature neurons are D1 and D2 medium spiny neurons (MSNs), respectively (Figures 2B and S2) (Gokce et al., 2016), which likely originate from the underlying striatum. It has been shown that acetyltransferase (ChAT)-positive neurons reside in the SVZ (Paez-Gonzalez et al., 2014). However, the only known marker for this SVZ-residing neuron type (*Chat*) was not detected in our dataset. We observed that a few cells of cluster 7 separated in tSNE space and were negative for D1 and D2 MSNs markers (Figure S2, red circle), indicating that they are a distinct neuron type and may represent SVZ-residing ChAT neurons.

Altogether, our comprehensive single-cell RNA profiling strategy enables the explicit identification of cell types based on numerous genes, gives an estimate of their relative proportions in the SVZ, and characterizes most neural and non-neural cell populations known to constitute the adult SVZ stem cell niche (for review, see Bjornsson et al., 2015; Bonaguidi et al., 2016) at unprecedented resolution. We provide an interactive and publicly available online tool (https://shiny.mdc-berlin.de/SVZapp/) for easy access to our data and visualization of gene expression in 9,804 individual cells.

RNA Dynamics Reveals Heterogeneity within the Neurogenic Lineage

To gain insight into the dynamics of stem cell activation and differentiation, we used velocyto (La Manno et al., 2018), a computational method that predicts the future state of individual cells from single-cell transcriptome data. The underlying assumption behind velocyto is that recent changes in the transcriptional rate of a gene, together with a simple maturation and turnover

Figure 2. Characterization of Cell Types Residing in the Adult SVZ

(A) tSNE plot of 9,804 cells colored by cluster annotation. The dendogram displays the relationships of cell clusters. Underlying boxes highlight main cell classes.

(B) Identification of cell types based on known marker genes. See also Figures S2 and S3.

(C) Heatmap depicting the expression of the top five enriched genes per cell type across all identified cells. Each row represents a single cell, and each column represents a gene. The expression is normalized by gene. For all significantly upregulated genes per cell type, see Table S1.

(D) tSNE plots of cells colored by expression of selected marker genes, which were used for the identification of astrocytes, NSCs, TAPs, and NBs. The color key indicates expression levels (red, high; yellow, low). The green circle highlights the absence of *Aqp4* in NSCs. The blue arrow indicates the expression of *Ascl1* in NSCs, which are close to TAPs. The purple arrow points to TAPs expressing *Dcx*.

SMCs, smooth muscle cells; PVMs, perivascular macrophages; MSNs, medium spiny neurons, which are contaminants from the striatum; COPs, differentiation-committed oligodendrocyte precursors; MOLs, mature oligodendrocytes; MFOLs, myelin-forming oligodendrocytes; NBs, neuroblasts; TAPs, transient amplifying progenitors; OPCs, oligodendrocyte progenitor cells; NSCs, neural stem cells. See also Figures S1, S2, and S3 and Tables S1 and S2.

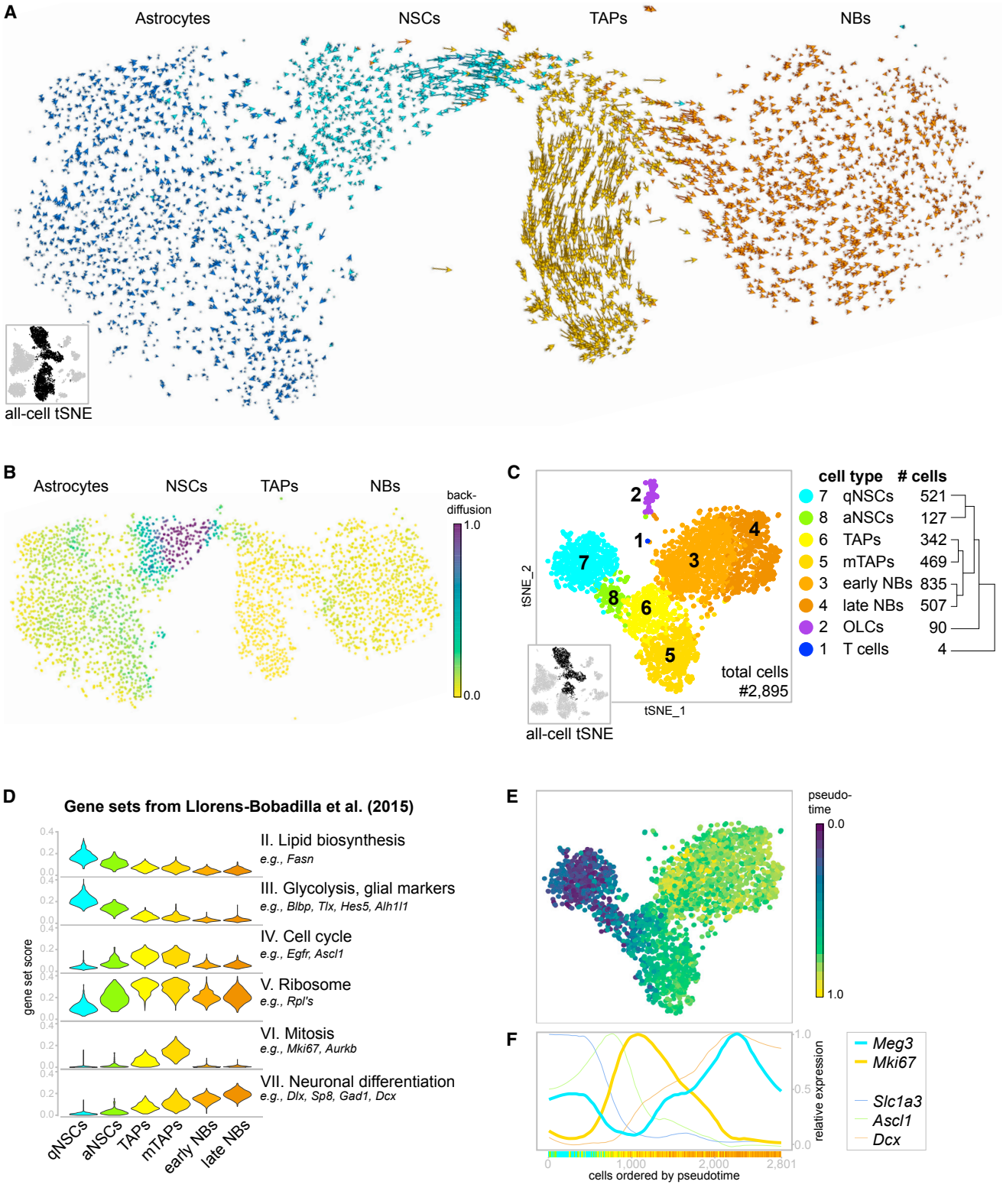

Figure 3. RNA Dynamics Reveal Heterogeneity within the Neurogenic Lineage

(A) RNA velocity plotted in tSNE space for astrocytes, NSCs, TAPs, and NBs (marked in black in the all-cell tSNE in the lower left). For each cell, arrows indicate the location of the estimated future cell state. RNA dynamics differ between cell clusters and within NSCs, TAPs, and NBs.

(legend continued on next page)

model, can be used to predict future up- or downregulation of the mature mRNA levels of that gene. These changes are estimated for each gene by calculating the ratio of unspliced to spliced reads in the sequencing data and fitting the parameters of the mRNA transcription, maturation, and turnover model of velocyto. The timescale of future predictions is on the scale of a few hours (La Manno et al., 2018).

We used velocyto to investigate the relationships among astrocytes, NSCs, TAPs, and NBs. We visualized the results in tSNE space by plotting an arrow for each cell, which spans the actual and the estimated future states (Figure 3A). Hence, cells that seemingly have either started or stopped to transcribe many genes have long arrows, whereas cells with overall small changes in RNA metabolism have short or no arrows. In the astrocyte cell cluster, we observed little and uncoordinated RNA velocity, indicating that these cells were in a transcriptionally stable state undergoing few changes. NSCs separated from the astrocyte cluster, demonstrating distinct transcriptome signatures. We observed differences in RNA dynamics within the NSC and neural progenitor clusters. RNA velocity was low in NSCs close to astrocytes, increased toward TAPs, and decreased in NBs. To gain higher resolution of cell types constituting the neurogenic lineage, we performed subclustering of NSCs, TAPs, and NBs (clusters 17, 14, and 13, respectively, in the all-cell tSNE) and obtained eight clusters, six of which represent different progenitor states along the neurogenic lineage (Figure 3C). Subcluster 1 was composed of contaminating T cells, whereas subcluster 2 contained oligodendrocyte-like cells (OLCs) (description in Figures S4C–S4E). Subclusters were composed of cells from all replicates with only slight differences in ratios in three of eight subclusters (Figures S4A and S4B). Subcluster-enriched genes are provided in Table S3.

To classify the six subclusters of the neurogenic lineage, we evaluated the expression of marker genes and scored the cells based on published gene sets (Llorens-Bobadilla et al., 2015) (Figure 3D). We identified quiescent NSCs (qNSCs) based on highest expression levels of genes associated with lipid biosynthesis, glycolysis, and glial markers. In activated NSCs (aNSCs), transcript levels of cell-cycle-associated and ribosomal genes started to increase and rose further in TAPs. Genes associated with mitosis were almost exclusively detected in subcluster 5, indicating that these cells are mitotic transient amplifying progenitors (mTAPs). In NBs, the expression of genes associated with cell cycle and mitosis decreased, while the expression of genes that function in neuronal differentiation increased. NBs formed two clusters. Neuronal genes were more lowly expressed in early compared to late NBs (Figure 3D). To analyze the progression of the cell cycle, we visualized cells within the S and G2M phases by summarizing expression values of respective genes from an independent gene list (Tirosh et al., 2016) (Figures S4G and S4H). The tSNE feature plots illustrated the entry of aNSCs into S phase, followed by TAPs, which showed high expression of S phase genes. S phase genes decreased toward the tip of the mTAP cluster: here, G2M genes displayed the highest expression.

The RNA velocity analysis revealed that NSCs have little RNA dynamics during quiescence but change their transcriptome vigorously within a few hours upon activation (Figure 3A). Most arrows pointed toward the NB cluster, and we observed little flow of aNSCs in the opposite direction, supporting the model that aNSCs do not divide asymmetrically, but mostly undergo consuming (=unidirectional) cell division to generate TAPs (Obernier et al., 2018). Arrows within TAPs pointed either toward NBs or to the bottom of the mTAP cluster, indicating that these cells were about to differentiate into NBs or to divide. mTAPs displayed the highest velocity, most likely resulting from their fast cycling nature. Most arrows in the NB cluster pointed away from NSCs and TAPs, depicting the direction of the differentiation process. Decreasing RNA dynamics toward late NBs made us speculate that cells in this differentiation state have a stable transcriptome in the SVZ but change their gene expression in the olfactory bulb, where they terminally differentiate.

We identified the root of the differentiation process in the NSC cluster (Figure 3B). Therefore, our RNA dynamics analysis independently confirms the marker-based identification of NSCs and highlights the direction of their differentiation fate via TAPs to NBs. This finding was supported by pseudotime analysis of the neurogenic lineage (subclusters 3–8, Figure 3E). Our RNA velocity analysis, in combination with subclustering, provided insights into the transcriptional dynamics of different NSC activation states and progeny subtypes. The continuity of cells in tSNE space (Figures 3A and 3C), together with the progression of both pseudotime (Figure 3E) and gene expression along cell types (Figures 3D and 3F), demonstrates that our dataset contains the entire neurogenic lineage, and illustrates the continuous nature of neurogenesis, which makes a rigid classification of distinct cell types along the differentiation trajectory difficult.

(B) The root of the differentiation process was identified in the NSC cluster by modeling the transition probabilities derived from the RNA velocity. The color scale represents the density of starting points of a reverse Markov process and ranges from low (yellow) to high (blue).

(C) Subclustering analysis of NSCs, TAPs, and NBs (marked in black in the all-cell tSNE in the lower left) revealed eight subclusters. The dendogram shows the relationships of cell types. Subclusters 1 and 2 are described in Figures S4C–S4E. Subclusters 3–8 belong to the neurogenic lineage and can be recognized by their RNA dynamics in the velocity tSNE depicted in (A).

(D) Cell-type characterization based on gene sets published in Llorens-Bobadilla et al. (2015).

(E) Pseudotime of the neurogenic lineage (subclusters 3–8, C) plotted in tSNE space. Pseudotime gradually increases from qNSCs to NBs via aNSCs, TAPs, and mTAPs. Blue indicates low and yellow indicates high pseudotime.

(F) Relative expression of selected genes across the cells of the neurogenic lineage ordered by pseudotime. The smooth lines were estimated by local regression (loess). Loess prediction has been scaled to 0–1 for each gene. Colors on the x axis indicate the subcluster (colors as in C and D). The long non-coding RNA (lncRNA) *Meg3* is negatively correlated with cell-cycle genes (here, *Mki67*). See also Figures S4E and S4G–S4I.

NSCs, neural stem cells; TAPs, transient amplifying progenitors; NBs, neuroblasts; qNSCs, quiescent neural stem cells; aNSCs, activated neural stem cells; mTAPs, mitotic transient amplifying progenitors; OLCs, oligodendrocyte-like cells. See also Figure S4 and Table S3.

Identification of NSC Activation-State Enriched Genes, Including lncRNAs

The comprehensiveness of our datasets enables evaluation of expression levels of cell-type-enriched genes in the context of the entire niche. At the moment, the discrimination of astrocytes, qNSCs, aNSCs, and TAPs based on single-marker genes is challenging. Manual inspection of cluster-enriched genes (Tables S2 and S3) revealed several candidates that might be involved in stem cell regulation and could be used to better discriminate NSCs from astrocytes and TAPs (Figure S4F). For example, the long non-coding RNA (lncRNA) *Meg3* is known to function as a negative regulator of growth (Zhou et al., 2012). In our dataset, it was highly expressed in mature neurons and detected in NSCs, NBs, OPCs, and ependymal cells. Surprisingly, it was absent from astrocytes and inversely correlated with genes associated with cell cycle, as well as mitosis (Figures 3F; S4E, blue background; and S4G–S4I). It would be interesting to investigate why *Meg3* is expressed in NSCs, but not in astrocytes. We hypothesize that it is involved in maintaining quiescence and preventing cells from entering the cell cycle.

SVZ and DG Cell-Type-Specific Signatures Correlate Well

To investigate the similarity of gene expression profiles of cell types constituting adult neurogenic niches, we compared our SVZ data with single-cell transcriptome data of the second neurogenic niche, the DG. We chose a DG dataset that characterizes the non-neuronal cellular components of this niche (Artegiani et al., 2017). Comparing the gene expression of cell clusters revealed high correlations for related cell types (Figure S4J). Because astrocytes and NSCs were combined in one cluster in the DG dataset (Artegiani et al., 2017), the coefficient of correlation was higher between SVZ astrocytes and DG NSCs than between SVZ qNSCs and DG NSCs. Cell types that were exclusively detected in the SVZ (e.g., ependymal cells and SMCs) did not correlate with any cell type of the DG, highlighting the accuracy of our comparison. The high similarity of gene expression profiles indicates common molecular features of cell types in both neurogenic niches.

Single-Cell RNA Profiling of LRP2-Deficient SVZ Reveals a Reduction of NSCs and Proliferating Cells

We asked whether an untargeted transcriptomic approach would be able to uncover cell-type-specific molecular defects underlying disturbances in adult SVZ neurogenesis. We used mice genetically deficient for expression of LRP2. LRP2, a member of the low-density lipoprotein receptor gene family, acts as an endocytic retrieval receptor for several signaling molecules and morphogens, including BMP4 and sonic hedgehog (SHH) (Christ et al., 2012, 2015; Gajera et al., 2010; Spoelgen et al., 2005). It plays central roles in controlling embryonic and adult neurogenesis (reviewed in Christ et al., 2016). With relevance to this study, LRP2 is highly expressed on the apical surface of ependymal cells in the adult SVZ, but not detected in the hippocampal neurogenic niche (SGZ) (Gajera et al., 2010). Adult LRP2-deficient mice display mild forebrain formation defects such as enlarged lumens of the lateral ventricles, but the ventricular system and ependymal architecture appeared normal in histological studies (Gajera et al., 2010). The number of NSCs and their progeny is significantly reduced, and neurogenesis is impaired specifically in the SVZ of adult LRP2-deficient mice (Gajera et al., 2010).

To pinpoint cell types that are specifically affected by LRP2 ablation, and to understand the underlying molecular causes, we performed single-cell RNA profiling of SVZs dissected from LRP2-deficient mice (knockout [KO]) and littermate controls (Ctr). We collected 8,056 cells in two replicates (Ctr and KO, four Drop-seq runs) (Figure S5A). Cell cluster proportions and relationships between cell types were similar for individual replicates (data not shown). Joint analysis of all samples resulted in the identification of 18 cell types (Figures 4A and S5B). Using a generalized linear mixed model to test biological variation independent from technical noise by modeling the genotype as fixed and the batch as random effect, we revealed a significant reduction in NSC proportions (p value < 0.001) (Figure S5C, right panel), which is in agreement with earlier observations obtained by targeted immunohistochemical approaches (Gajera et al., 2010). Apart from this finding, we did not observe discernable differences in cluster proportions based on batch or genotype (Figures S5A and S5C).

We compared the combined LRP2 KO/Ctr data (dataset B, Figure 4A) with our previous results (dataset A, Figure 2A) and observed only mild differences. Pericytes and SMCs belonged to one cluster (called mural cells), whereas mature neurons formed three clusters comprising potential ChAT neurons, D1 and D2 MSNs (Figure 4A). As in dataset A, potential ChAT neurons (cluster 12 in dataset B) expressed markers of mature neurons, but markers of striatal neurons were not detected (Figure S5B). Manual inspection of genes discriminating these neurons from D1 and D2 MSNs revealed five candidates that could serve as new markers (*Kit*, *Nxph1*, *Pthlh*, *Crtac1*, and *Sparcl1*) for this particular cell type (Figure S5D). Furthermore, we detected OLCs in an individual cluster and one cluster comprising choroid plexus cells (Figures 4A and S5B). As in dataset A, subclustering of NSCs, TAPs, and NBs resolved the different stages of neurogenesis (data not shown). The similarity of dataset A and dataset B demonstrates the robustness of our method, making it suitable to obtain and compare data from different mouse strains and genotypes.

Cells in the adult SVZ proliferate less in LRP2-deficient mice (Gajera et al., 2010). To analyze which cell types are affected, we scored cells according to cell cycle using a list of cell-cycle-associated genes (Tirosh et al., 2016) and plotted the cumulative fraction distributions per genotype and cell cluster. We quantified significantly less expressed cell-cycle genes in TAPs derived from mutant mice compared to control cells (p value < 0.01) (Figures 4B and S6A). The overall number of TAPs in our sequencing data did not change, indicating that LRP2-deficient mice had the same number of progenitors but TAPs had a reduced proliferation activity. To quantify proliferating cells in the SVZ, we treated LRP2-deficient mice and littermate controls with a single intraperitoneal injection of bromodeoxyuridine (BrdU) and sacrificed the animals 24 hr later. This protocol preferentially labels TAPs in this niche (Ponti et al., 2013). Counting BrdU-positive cells per ventral SVZ section confirmed a significant reduction of proliferating TAPs in LRP2-deficient mice (Figures 4C and 4D).

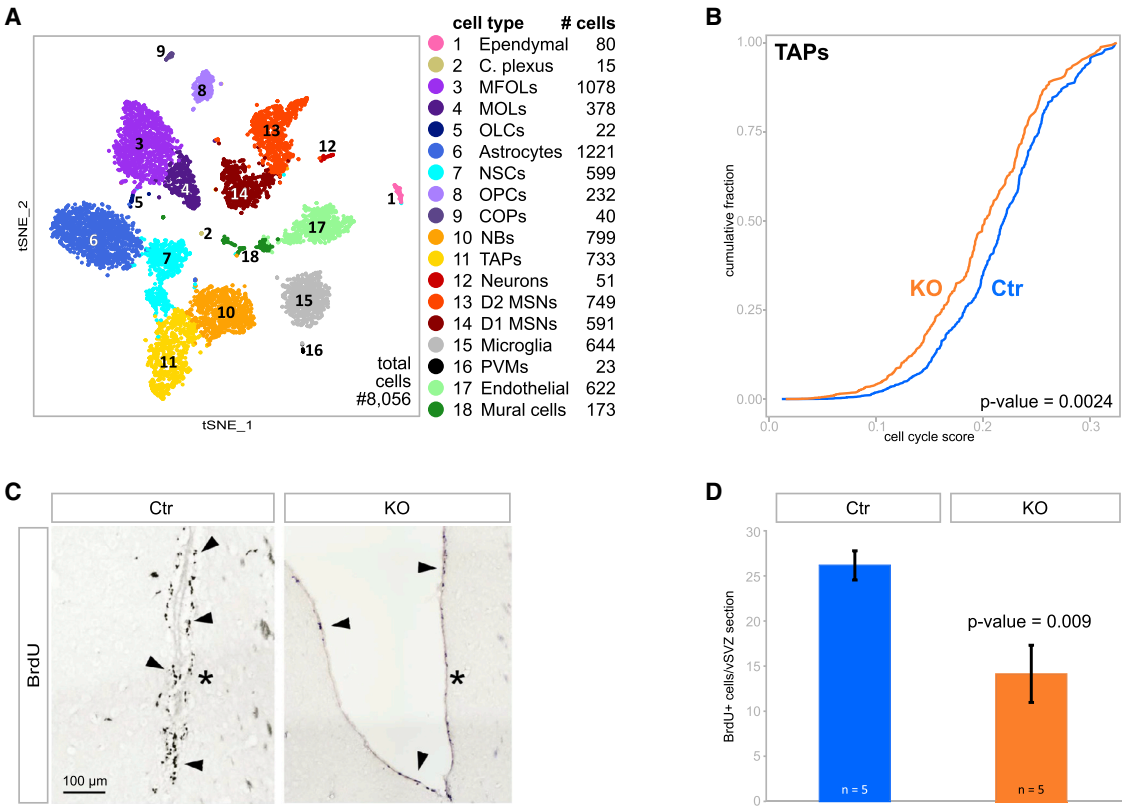

Figure 4. Cell Proliferation Is Reduced in the SVZ of LRP2-Deficient Mice

(A) tSNE plot of 8,056 cells from the SVZ of LRP2-deficient mice and littermate controls, colored by cluster annotation. For cell-type identification, see Figure S5B.

(B) Cumulative fraction of LRP2 KO and control (Ctr) TAPs scored for cell cycle. The statistical significance of data was determined using a Kolmogorov-Smirnov test. For the p values of the proliferation analysis for all cell types, see Figure S6A.

(C) Immunohistological detection of BrdU+ cells in the ventral (v) SVZ of KO and Ctr mice. BrdU+ cells are highlighted by arrowheads. Asterisks label the lateral ventricular wall.

(D) Quantification of the number of BrdU+ cells in the vSVZ 24 hr after BrdU injection (as exemplified in C). Mean values ± SEM were determined by counting the number of BrdU+ cells on 12 sections for each animal (five animals per genotype). The statistical significance of data was determined using an unpaired Student's t test.

C. plexus, choroid plexus; OLCs, oligodendrocyte-like cells; other cell-type abbreviations as in Figure 2; vSVZ, ventral SVZ; KO, LRP2-deficient mice; Ctr, wild-type and heterozygous littermate controls. See also Figures S5 and S6.

Cell-Type-Specific Differential Gene Expression Analysis Revealed Perturbations in BMP and Wnt Signaling and a Reduction in Ribosomal Gene Expression in LRP2-Deficient Mice

To identify cell-type-specific molecular changes underlying impaired adult SVZ neurogenesis in LRP2-deficient mice, we performed differential gene expression analysis per cell cluster. We analyzed the two replicates independently (an007_WT versus an007_KO and an010_WT versus an010_KO) and considered only genes with a p value smaller than 0.01 and a consistent fold change in both replicates as differentially expressed (Table S4). The results for NSCs, TAPs, and NBs are displayed in Figures 5A–5C. We found *Id3*, a downstream target of BMP signaling, upregulated in LRP2-mutant mice, in agreement with earlier findings using semiquantitative immunohistology (Gajera et al., 2010). *Id3* mRNA was specifically elevated in NBs derived from the LRP2-deficient SVZ (Figure 5C, green box). Increased immunostaining for ID3 protein in mutant mouse brain sections confirmed this result (Figures 5E and 5F). Furthermore, we found Catenin Beta 1 (*Ctnnb1*) to be decreased in TAPs of LRP2-mutant mice (Figure 5B, blue box). The Wnt/β-catenin pathway is known to stimulate NSC proliferation and self-renewal (Qu et al., 2010) but has not been linked to LRP2 activity so far. However, as the numbers of dividing cells and NSCs are decreased in LRP2-deficient mice, it is likely that LRP2 interacts not only with BMP4 and SHH (Christ et al., 2012, 2015; Gajera et al., 2010; Spoelgen et al., 2005) but also with other morphogens, including Wnt, which is known to regulate adult neurogenesis. To substantiate a role for LRP2 in Wnt signaling in the SVZ, we crossed the LRP2-mutant strain with a *Tcf/Lef_LacZ* reporter line commonly used to monitor Wnt/β-catenin signaling activity *in vivo* (Mohamed et al., 2004). Immunohistochemistry of SVZ sections revealed reduced *Tcf/Lef_LacZ* activity in LRP2-deficient mice compared to littermate controls (Figure 5D).

Among the downregulated genes in TAPs and NBs obtained from LRP2-mutant SVZ, we observed many genes encoding

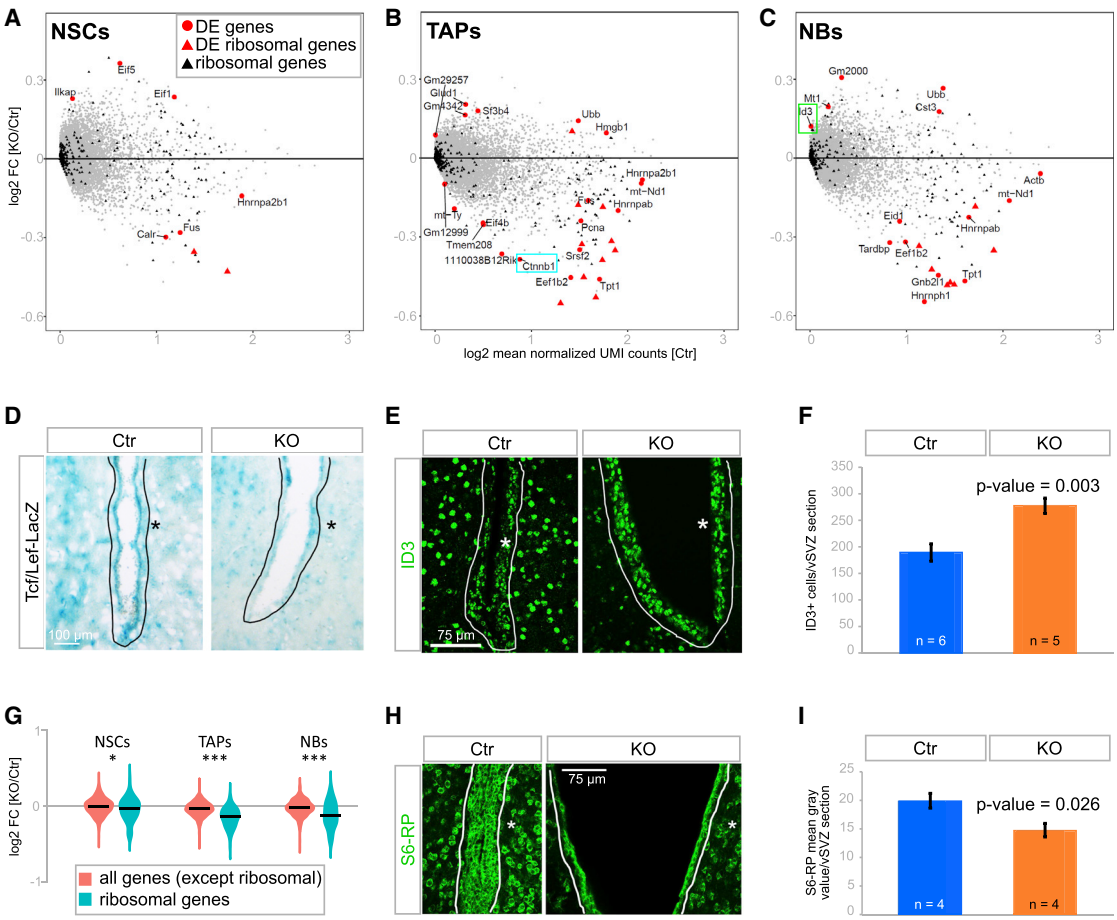

Figure 5. Differential Gene Expression Analysis per Cell Type Reveals Perturbations in BMP and Wnt Signaling and a Reduction of Ribosomal Genes in LRP2-Deficient Mice

(A–C) Comparison of gene expression KO versus Ctr in NSCs (A), TAPs (B), and NBs (C). Ribosomal genes are depicted as triangles. Significantly differential genes are marked in red, and non-ribosomal genes are named. The blue box highlights the decrease of *Ctnnb1* in TAPs (B). The green box highlights the increase of *Id3* in NBs (C). Significantly changed genes for cell types identified in Figure 4A are listed in Table S4. Differential gene expression analysis was performed using edgeR.

(D) Staining for LacZ activity (blue) on sections of the vSVZ of *Tcf/Lef_LacZ* mice, either Ctr or KO for *Lrp2*. Exemplary images from four mice per genotype are shown (three sections per animal were evaluated).

(E) Immunohistological detection of ID3 (green) in the vSVZ of Ctr or KO mice.

(F) Quantification of the number of ID3+ cells in the vSVZ of Ctr and KO mice (as exemplified in E). Three sections each from five KO mice and six Ctr mice were analyzed.

(G) Distribution of log2 fold changes (LRP2 KO versus Ctr, cells averaged per cluster) of ribosomal genes (teal) and all remaining genes (red) for NSCs, TAPs, and NBs. Expression cutoff $\geq$ 0.5 log2 (mean normalized UMI count) Ctr cells. *$p < 0.05$, ***$p < 0.001$, unpaired Student's t test. For comparison of all cell types, see Figures S6B and S6C.

(H) Immunohistological detection of ribosomal protein S6 (S6-RP, green) in the vSVZ of Ctr or KO mice.

(I) Quantification of S6-RP expression levels in the vSVZ of Ctr and KO mice (as exemplified in H). Values are given as mean fluorescence intensities. Three sections each from four mice per genotype were quantified.

(D, E, H) Solid lines mark the SVZ. Asterisks label the lateral ventricular wall. (F, I) Depicted are mean values ± SEM. The statistical significance of data was determined using an unpaired Student's t test. FC, fold change; DE, differential expressed; NSCs, neural stem cells; TAP, transient amplifying progenitors; NBs, neuroblasts; KO, LRP2-deficient mice; Ctr, wild-type and heterozygous littermate controls; vSVZ, ventral subventricular zone; S6-RP, ribosomal protein S6. See also Figure S6 and Table S4.

ribosomal subunits (Figures 5B and 5C, triangles). To investigate whether this is a cell-type-specific trend, we compared the expression of ribosomal genes to the expression of all remaining genes per cell type. In 10 of the 18 identified cell types, ribosomal genes were significantly reduced, indicating a broad effect of LRP2-deficiency on ribosomal biogenesis in multiple cell types residing in the SVZ neurogenic niche (Figures 5G and S6B). However, TAPs had by far the lowest p value (Figure S6C), which is consistent with the observed reduction in cell proliferation. To confirm the detected reduction of ribosomal genes, we exemplarily stained for the ribosomal protein S6 (S6-RP) and measured the relative signal intensity per SVZ section. We found a significant reduction in the amount of S6-RP in the SVZ of LRP2-deficient mice compared to littermate controls (Figures 5H and 5I).

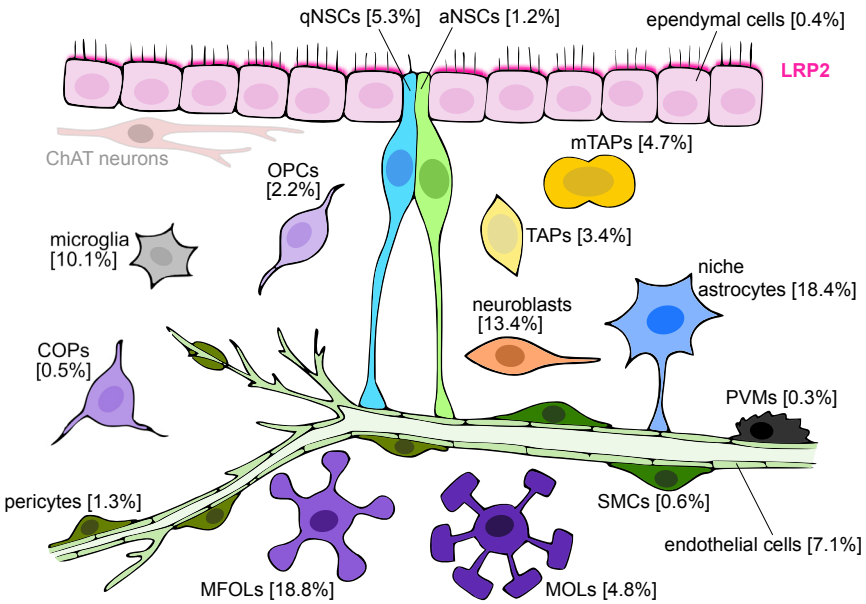

Figure 6. Cellular Composition of the Adult SVZ Neurogenic Niche and Expression of LRP2

Illustration of cell types residing in the SVZ. Cells depicted with a black outline were characterized in this study. Numbers in brackets are the mean of the obtained cell-type proportions (Figures S1D and S4B). ChAT neurons (gray outline) could not be identified unambiguously in our data. LRP2, marked in red, is specifically expressed in ependymal cells (Gajera et al., 2010). qNSCs, quiescent neural stem cells; aNSCs, activated neural stem cells; TAPs, transient amplifying progenitors; mTAPs, mitotic transient amplifying progenitors; PVMs, perivascular macrophages; SMCs, smooth muscle cells; OPCs, oligodendrocyte progenitor cells; COPs, differentiation-committed oligodendrocyte precursors; MFOLs, myelin-forming oligodendrocytes; MOLs, mature oligodendrocytes.

Altogether, differential gene expression analysis confirmed known defects in BMP signaling and identified a new signaling pathway (Wnt) to be perturbed in LRP2-deficient mice. In both cases, our analysis was able to newly assign these signaling defects to distinct cell types in the SVZ niche.

DISCUSSION

The SVZ of the lateral ventricles is the largest germinal region in the adult rodent brain. However, a comprehensive catalog that molecularly profiles all cell types of this niche has not existed until now. In 1997, Doetsch and colleagues published a study addressing the cellular composition of the SVZ. Based on ultrastructure and a few marker genes, they identified seven cell types, but several important and acknowledged niche populations (i.e., vascular cells) were not reported (Doetsch et al., 1997). Further studies focused on discrete cell types, for example, microglia (Ribeiro Xavier et al., 2015) or endothelial and other vascular cells (Shen et al., 2004, 2008). But to the best of our knowledge, no publication as yet characterizes all SVZ cells together and gives an up-to-date estimate of the cell-type proportions. In the literature, the size of a given cell population depends on the choice of marker genes used for identification. For example, qNSCs are identified and isolated by co-expression of GFAP and PROM1, but not EGFR (Fischer et al., 2011). However, there is evidence for the existence of PROM1-negative qNSCs (Codega et al., 2014; Obernier et al., 2018), which in turn are difficult to distinguish from niche astrocytes. Here, instead of classifying cells based on a few selected marker genes, we used genome-wide expression profiling to cluster cells by transcriptome similarity and uncover cell identities by analyzing a multitude of genes. Because the SVZ is not an enclosed tissue, it is challenging to obtain absolute numbers of the cellular composition. Nevertheless, our study gives a marker-independent estimate on the abundances of cell types residing in the adult SVZ neurogenic niche (Figures 6, S1D, and S4B) and provides their gene expression signatures. An interactive online tool makes our data readily and publicly accessible and allows browsing of genes of interest in the context of 22 cell types.

Consistent with previous single-cell RNA sequencing studies (Basak et al., 2018; Dulken et al., 2017; Llorens-Bobadilla et al., 2015), we resolved different NSC activation states (Figure 3). In addition, our data allowed us to distinguish between niche astrocytes and NSCs (Figures 2 and 3A). The cell-type-enriched genes identified in this study comprised both interesting candidates that might be involved in stem cell regulation, and potential new markers that could advance discrimination of niche populations, as well as different NSCs states. RNA velocity analysis (Figures 3A and 3B) revealed that astrocytes and qNSCs have rather stable transcriptomes, whereas aNSCs are about to change their gene expression signature and move uniformly toward the TAP state. mTAPs underwent vigorous transcriptomic changes, probably due to their actively dividing state. Movements decreased from early to late NBs and made us hypothesize that progenitors in the SVZ have a less dynamic transcriptome once they acquired the NB fate. It is likely that RNA dynamics increase again when NBs reach the olfactory bulb, where they terminally differentiate into interneurons. Additional experiments resulting in deeper single-cell RNA sequencing data may lead to an even finer resolution of the neurogenic lineage. Applying Div-seq (Habib et al., 2016), a method that combines single-nucleus RNA sequencing and pulse labeling of dividing cells with 5-ethylenyl-2′-deoxyuridine (EdU), could be used to enrich for cells of the neurogenic lineage. Sequencing single nuclei instead of single cells could potentially enrich the amount of sequenced unspliced reads and therefore advance the RNA velocity analysis.

NSCs have been postulated to be tri-potent and capable of generating neurons, oligodendrocytes, and astrocytes. This assumption has been largely based on *in vitro* experiments, which demonstrated that adult NSCs are able to self-renew

and to produce different cell types (Reynolds and Weiss, 1992; reviewed in Pastrana et al., 2011). *In vivo* population fate-mapping studies showed that SVZ NSCs give rise to OPCs and MOLs (Menn et al., 2006), but clonal analysis revealed only the production of interneurons from individual NSCs (Calzolari et al., 2015). Along this line, the sequencing data, which reflect a snapshot of processes taking place *in vivo*, revealed the neurogenic lineage, but no connection between NSCs and OPCs. However, because oligodendrogenesis is a rare event (Menn et al., 2006), it is conceivable that despite the vast cell-type coverage and high resolution of our dataset, the sampling was not dense enough to capture intermediate cells that support this process. Because single-cell RNA sequencing methods and computational tools are developing rapidly (reviewed in Kester and van Oudenaarden, 2018), *in silico* lineage tracing of adult NSCs will most likely improve.

Conceptually, our untargeted single-cell transcriptomic approach facilitates the study of the SVZ in mouse models with disturbed adult neurogenesis, as shown for LRP2-deficient mice herein. LRP2 is an endocytic receptor expressed in specialized absorptive epithelia, including the ependymal layer facing the SVZ neurogenic niche. The receptor acts a multiligand clearance receptor that regulates the extracellular concentration of essential metabolites and signaling molecules available to surrounding target cells (reviewed in Willnow and Christ, 2017). Although a function of LRP2 in the ependyma in regulating the milieu of the SVZ neurogenic niche has been appreciated (Gajera et al., 2010), the exact nature of the signaling molecules (and their downstream effects) controlled by LRP2 remained unclear. Our findings uncovered alterations in BMP and Wnt signaling in target cells of the niche as a consequence of LRP2 deficiency (Figure 5). These findings are most consistent with a model whereby impaired clearance of these morphogens by LRP2 in the ependyma alters BMP and Wnt concentrations. Hence, signal reception in other cell types in the niche is perturbed, affecting cellular metabolism (e.g., protein biosynthesis) (Figures 5, S6B, and S6C) and proliferative capacity (Figure 4). The ability of LRP2 to act as a clearance receptor for BMPs has been shown by us before (Gajera et al., 2010; Spoelgen et al., 2005). The potential of this receptor to act as a receptor for Wnt ligands is supported by the function of the related Wnt receptors LRP5 and LRP6 (reviewed in MacDonald and He, 2012). Alternatively, the loss of Wnt signals in the LRP2-deficient SVZ may be a secondary consequence of alterations of other morphogen pathways affected by this receptor. Such an effect has been documented in the developing retina, where loss of LRP2 aberrantly increases SHH activity, which in turn results in loss of Wnt signals (Christ et al., 2015).

Altogether, our proof of concept experiment provides insights into the regulation of SVZ neurogenesis by LRP2 and demonstrates the applicability of single-cell transcriptomics to study complex tissues obtained from gene-targeted mouse models. By analyzing single-cell RNA sequencing data, we revealed changes in cell-type proportions, proliferation activity, and signaling pathways. The variety of obtained results highlights the power of our approach in elucidating consequences of loss-of-function mutations in an efficient, comprehensive, and untargeted way.

STAR★METHODS

Detailed methods are provided in the online version of this paper and include the following:

- KEY RESOURCES TABLE
- CONTACT FOR REAGENT AND RESOURCE SHARING
- EXPERIMENTAL MODEL AND SUBJECT DETAILS
  - Animals
- METHOD DETAILS
  - Generation of SVZ single-cell suspension
  - Fixation and rehydration of cells for Drop-seq
  - Drop-seq run
  - Assessment of droplet quality
  - Droplet Breakage
  - Single-cell library generation and sequencing
  - BrdU labeling experiments
  - Immunohistology
  - LacZ staining
- QUANTIFICATION AND STATISTICAL ANALYSIS
  - Definition of significance
  - Drop-seq computational pipeline: Data processing, alignment and gene quantification
  - Cell and gene filtering
  - Normalization, clustering, marker discovery, and data visualization
  - RNA velocity analysis
  - Subclustering
  - Diffusion pseudotime analysis
  - Gene set scoring
  - Comparison gene expression profiles
  - Proliferation analysis of cells derived from LRP2-deficient versus Ctr SVZ (dataset B)
  - Differential gene expression analysis of cells derived from LRP2-deficient versus Ctr SVZ
  - Ribosomal gene expression comparison of cells derived from LRP2-deficient versus Ctr SVZ
  - Generalized linear mixed model
  - Statistical analysis of immunohistochemistry data
- DATA AND SOFTWARE AVAILABILITY
- ADDITIONAL RESOURCES

SUPPLEMENTAL INFORMATION

Supplemental Information includes six figures and four tables and can be found with this article online at https://doi.org/10.1016/j.celrep.2018.11.003.

ACKNOWLEDGMENTS

We thank Susanne A. Wolf for help with animal experiments and optimizing tissue dissociation; Christine Kocks for guidance and support with single-cell transcriptome profiling; Anastasiya Boltengagen, Salah Ayoub, and Maria Schmeisser for technical support; Sten Linnarsson and Gioele La Manno for help with the velocyto.py package; and F. Alexander Wolf for discussing lineage tracing, as well as pseudotime tools. We thank Christine Kocks and Monika Piwecka for critically reading the manuscript and the entire Rajewsky lab for discussions, helpful comments, and sharing code. A.M. acknowledges funding from the European Union's Horizon 2020 research and innovation program, under the Marie Sklodowska-Curie Actions (MSCA) grant

(721890). N.R. acknowledges funding from the Chan Zuckerberg Initiative, an advised fund of Silicon Valley Community Foundation.

AUTHOR CONTRIBUTIONS

Conceptualization, V.Z., and N.R.; Software, A.M. and V.Z.; Validation, V.Z. and L.B.; Formal Analysis, A.M., V.Z., L.B., and N.R.; Investigation, V.Z. and L.B.; Data Curation, A.M.; Writing – Original Draft, V.Z.; Writing – Review & Editing, V.Z., A.M., T.E.W., and N.R.; Visualization, V.Z. and A.M.; Supervision, N.R. and T.E.W.; Funding Acquisition, N.R. and T.E.W.

DECLARATION OF INTERESTS

The authors declare no competing interests.

Received: July 9, 2018
Revised: September 13, 2018
Accepted: October 31, 2018
Published: November 27, 2018

REFERENCES

Alles, J., Karaiskos, N., Praktiknjo, S.D., Grosswendt, S., Wahle, P., Ruffault, P.-L., Ayoub, S., Schreyer, L., Boltengagen, A., Birchmeier, C., et al. (2017). Cell fixation and preservation for droplet-based single-cell transcriptomics. BMC Biol. *15*, 44.

Artegiani, B., Lyubimova, A., Muraro, M., van Es, J.H., van Oudenaarden, A., and Clevers, H. (2017). A single-cell RNA sequencing study reveals cellular and molecular dynamics of the hippocampal neurogenic niche. Cell Rep. *21*, 3271–3284.

Basak, O., Krieger, T.G., Muraro, M.J., Wiebrands, K., Stange, D.E., Frias-Aldeguer, J., Rivron, N.C., van de Wetering, M., van Es, J.H., van Oudenaarden, A., et al. (2018). Troy+ brain stem cells cycle through quiescence and regulate their number by sensing niche occupancy. Proc. Natl. Acad. Sci. USA *115*, E610–E619.

Bates, D., Mächler, M., Bolker, B., and Walker, S. (2015). Fitting linear mixed-effects models using lme4. J. Stat. Softw. *67*, 1–48.

Beckervordersandforth, R., Tripathi, P., Ninkovic, J., Bayam, E., Lepier, A., Stempfhuber, B., Kirchhoff, F., Hirrlinger, J., Haslinger, A., Lie, D.C., et al. (2010). *In vivo* fate mapping and expression analysis reveals molecular hallmarks of prospectively isolated adult neural stem cells. Cell Stem Cell *7*, 744–758.

Bjornsson, C.S., Apostolopoulou, M., Tian, Y., and Temple, S. (2015). It takes a village: constructing the neurogenic niche. Dev. Cell *32*, 435–446.

Bonaguidi, M.A., Stadel, R.P., Berg, D.A., Sun, J., Ming, G.L., and Song, H. (2016). Diversity of neural precursors in the adult mammalian brain. Cold Spring Harb. Perspect. Biol. *8*, a018838.

Calzolari, F., Michel, J., Baumgart, E.V., Theis, F., Götz, M., and Ninkovic, J. (2015). Fast clonal expansion and limited neural stem cell self-renewal in the adult subependymal zone. Nat. Neurosci. *18*, 490–492.

Chaker, Z., Codega, P., and Doetsch, F. (2016). A mosaic world: puzzles revealed by adult neural stem cell heterogeneity. Wiley Interdiscip. Rev. Dev. Biol. *5*, 640–658.

Christ, A., Christa, A., Kur, E., Lioubinski, O., Bachmann, S., Willnow, T.E., and Hammes, A. (2012). LRP2 is an auxiliary SHH receptor required to condition the forebrain ventral midline for inductive signals. Dev. Cell *22*, 268–278.

Christ, A., Christa, A., Klippert, J., Eule, J.C., Bachmann, S., Wallace, V.A., Hammes, A., and Willnow, T.E. (2015). LRP2 acts as SHH clearance receptor to protect the retinal margin from mitogenic stimuli. Dev. Cell *35*, 36–48.

Christ, A., Herzog, K., and Willnow, T.E. (2016). LRP2, an auxiliary receptor that controls sonic hedgehog signaling in development and disease. Dev. Dyn. *245*, 569–579.

Codega, P., Silva-Vargas, V., Paul, A., Maldonado-Soto, A.R., Deleo, A.M., Pastrana, E., and Doetsch, F. (2014). Prospective identification and purification of quiescent adult neural stem cells from their *in vivo* niche. Neuron *82*, 545–559.

Dobin, A., Davis, C.A., Schlesinger, F., Drenkow, J., Zaleski, C., Jha, S., Batut, P., Chaisson, M., and Gingeras, T.R. (2013). STAR: ultrafast universal RNA-seq aligner. Bioinformatics *29*, 15–21.

Doetsch, F., García-Verdugo, J.M., and Alvarez-Buylla, A. (1997). Cellular composition and three-dimensional organization of the subventricular germinal zone in the adult mammalian brain. J. Neurosci. *17*, 5046–5061.

Doetsch, F., Caillé, I., Lim, D.A., García-Verdugo, J.M., and Alvarez-Buylla, A. (1999). Subventricular zone astrocytes are neural stem cells in the adult mammalian brain. Cell *97*, 703–716.

Dubreuil, V., Marzesco, A.-M., Corbeil, D., Huttner, W.B., and Wilsch-Bräuninger, M. (2007). Midbody and primary cilium of neural progenitors release extracellular membrane particles enriched in the stem cell marker prominin-1. J. Cell Biol. *176*, 483–495.

Dulken, B.W., Leeman, D.S., Boutet, S.C., Hebestreit, K., and Brunet, A. (2017). Single-cell transcriptomic analysis defines heterogeneity and transcriptional dynamics in the adult neural stem cell lineage. Cell Rep. *18*, 777–790.

Fischer, J., Beckervordersandforth, R., Tripathi, P., Steiner-Mezzadri, A., Ninkovic, J., and Götz, M. (2011). Prospective isolation of adult neural stem cells from the mouse subependymal zone. Nat. Protoc. *6*, 1981–1989.

Gajera, C.R., Emich, H., Lioubinski, O., Christ, A., Beckervordersandforth-Bonk, R., Yoshikawa, K., Bachmann, S., Christensen, E.I., Götz, M., Kempermann, G., et al. (2010). LRP2 in ependymal cells regulates BMP signaling in the adult neurogenic niche. J. Cell Sci. *123*, 1922–1930.

Gokce, O., Stanley, G.M., Treutlein, B., Neff, N.F., Camp, J.G., Malenka, R.C., Rothwell, P.E., Fuccillo, M.V., Südhof, T.C., and Quake, S.R. (2016). Cellular taxonomy of the mouse striatum as revealed by single-cell RNA-seq. Cell Rep. *16*, 1126–1137.

Guez-Barber, D., Fanous, S., Harvey, B.K., Zhang, Y., Lehrmann, E., Becker, K.G., Picciotto, M.R., and Hope, B.T. (2012). FACS purification of immunolabeled cell types from adult rat brain. J. Neurosci. Methods *203*, 10–18.

Habib, N., Li, Y., Heidenreich, M., Swiech, L., Avraham-Davidi, I., Trombetta, J.J., Hession, C., Zhang, F., and Regev, A. (2016). Div-seq: single-nucleus RNA-seq reveals dynamics of rare adult newborn neurons. Science *353*, 925–928.

Haghverdi, L., Büttner, M., Wolf, F.A., Buettner, F., and Theis, F.J. (2016). Diffusion pseudotime robustly reconstructs lineage branching. Nat. Methods *13*, 845–848.

Kantarci, S., Al-Gazali, L., Hill, R.S., Donnai, D., Black, G.C.M., Bieth, E., Chassaing, N., Lacombe, D., Devriendt, K., Teebi, A., et al. (2007). Mutations in LRP2, which encodes the multiligand receptor megalin, cause Donnai-Barrow and facio-oculo-acoustico-renal syndromes. Nat. Genet. *39*, 957–959.

Kester, L., and van Oudenaarden, A. (2018). Single-cell transcriptomics meets lineage tracing. Cell Stem Cell *23*, 166–179.

La Manno, G., Soldatov, R., Zeisel, A., Braun, E., Hochgerner, H., Petukhov, V., Lidschreiber, K., Kastriti, M.E., Lönnerberg, P., Furlan, A., et al. (2018). RNA velocity of single cells. Nature *560*, 494–498.

Lein, E.S., Hawrylycz, M.J., Ao, N., Ayres, M., Bensinger, A., Bernard, A., Boe, A.F., Boguski, M.S., Brockway, K.S., Byrnes, E.J., et al. (2007). Genome-wide atlas of gene expression in the adult mouse brain. Nature *445*, 168–176.

Llorens-Bobadilla, E., Zhao, S., Baser, A., Saiz-Castro, G., Zwadlo, K., and Martin-Villalba, A. (2015). Single-cell transcriptomics reveals a population of dormant neural stem cells that become activated upon brain injury. Cell Stem Cell *17*, 329–340.

Luo, Y., Coskun, V., Liang, A., Yu, J., Cheng, L., Ge, W., Shi, Z., Zhang, K., Li, C., Cui, Y., et al. (2015). Single-cell transcriptome analyses reveal signals to activate dormant neural stem cells. Cell *161*, 1175–1186.

MacDonald, B.T., and He, X. (2012). Frizzled and LRP5/6 receptors for Wnt/β-catenin signaling. Cold Spring Harb. Perspect. Biol. *4*, a007880.

Macosko, E.Z., Basu, A., Satija, R., Nemesh, J., Shekhar, K., Goldman, M., Tirosh, I., Bialas, A.R., Kamitaki, N., Martersteck, E.M., et al. (2015). Highly parallel genome-wide expression profiling of individual cells using nanoliter droplets. Cell *161*, 1202–1214.

Marques, S., Zeisel, A., Codeluppi, S., van Bruggen, D., Mendanha Falcão, A., Xiao, L., Li, H., Häring, M., Hochgerner, H., Romanov, R.A., et al. (2016). Oligodendrocyte heterogeneity in the mouse juvenile and adult central nervous system. Science *352*, 1326–1329.

Menn, B., Garcia-Verdugo, J.M., Yaschine, C., Gonzalez-Perez, O., Rowitch, D., and Alvarez-Buylla, A. (2006). Origin of oligodendrocytes in the subventricular zone of the adult brain. J. Neurosci. *26*, 7907–7918.

Ming, G.-L., and Song, H. (2011). Adult neurogenesis in the mammalian brain: significant answers and significant questions. Neuron *70*, 687–702.

Mohamed, O.A., Clarke, H.J., and Dufort, D. (2004). Beta-catenin signaling marks the prospective site of primitive streak formation in the mouse embryo. Dev. Dyn. *231*, 416–424.

Obernier, K., Cebrian-Silla, A., Thomson, M., Parraguez, J.I., Anderson, R., Guinto, C., Rodas Rodriguez, J., Garcia-Verdugo, J.-M., and Alvarez-Buylla, A. (2018). Adult neurogenesis is sustained by symmetric self-renewal and differentiation. Cell Stem Cell *22*, 221–234.

Paez-Gonzalez, P., Asrican, B., Rodriguez, E., and Kuo, C.T. (2014). Identification of distinct ChAT^{+} neurons and activity-dependent control of postnatal SVZ neurogenesis. Nat. Neurosci. *17*, 934–942.

Pastrana, E., Silva-Vargas, V., and Doetsch, F. (2011). Eyes wide open: a critical review of sphere-formation as an assay for stem cells. Cell Stem Cell *8*, 486–498.

Ponti, G., Obernier, K., Guinto, C., Jose, L., Bonfanti, L., and Alvarez-Buylla, A. (2013). Cell cycle and lineage progression of neural progenitors in the ventricular-subventricular zones of adult mice. Proc. Natl. Acad. Sci. USA *110*, E1045–E1054.

Qu, Q., Sun, G., Li, W., Yang, S., Ye, P., Zhao, C., Yu, R.T., Gage, F.H., Evans, R.M., and Shi, Y. (2010). Orphan nuclear receptor TLX activates Wnt/beta-catenin signalling to stimulate neural stem cell proliferation and self-renewal. Nat. Cell Biol. *12*, 31–40.

Reynolds, B.A., and Weiss, S. (1992). Generation of neurons and astrocytes from isolated cells of the adult mammalian central nervous system. Science *255*, 1707–1710.

Ribeiro Xavier, A.L., Kress, B.T., Goldman, S.A., Lacerda de Menezes, J.R., and Nedergaard, M. (2015). A distinct population of microglia supports adult neurogenesis in the subventricular zone. J. Neurosci. *35*, 11848–11861.

Robinson, M.D., McCarthy, D.J., and Smyth, G.K. (2010). edgeR: a Bioconductor package for differential expression analysis of digital gene expression data. Bioinformatics *26*, 139–140.

Satija, R., Farrell, J.A., Gennert, D., Schier, A.F., and Regev, A. (2015). Spatial reconstruction of single-cell gene expression data. Nat. Biotechnol. *33*, 495–502.

Shah, P.T., Stratton, J.A., Stykel, M.G., Abbasi, S., Sharma, S., Mayr, K.A., Koblinger, K., Whelan, P.J., and Biernaskie, J. (2018). Single-cell transcriptomics and fate mapping of ependymal cells reveals an absence of neural stem cell function. Cell *173*, 1045–1057.

Shen, Q., Goderie, S.K., Jin, L., Karanth, N., Sun, Y., Abramova, N., Vincent, P., Pumiglia, K., and Temple, S. (2004). Endothelial cells stimulate self-renewal and expand neurogenesis of neural stem cells. Science *304*, 1338–1340.

Shen, Q., Wang, Y., Kokovay, E., Lin, G., Chuang, S.-M., Goderie, S.K., Roysam, B., and Temple, S. (2008). Adult SVZ stem cells lie in a vascular niche: a quantitative analysis of niche cell-cell interactions. Cell Stem Cell *3*, 289–300.

Shin, J., Berg, D.A., Zhu, Y., Shin, J.Y., Song, J., Bonaguidi, M.A., Enikolopov, G., Nauen, D.W., Christian, K.M., Ming, G.L., and Song, H. (2015). Single-cell RNA-seq with waterfall reveals molecular cascades underlying adult neurogenesis. Cell Stem Cell *17*, 360–372.

Spoelgen, R., Hammes, A., Anzenberger, U., Zechner, D., Andersen, O.M., Jerchow, B., and Willnow, T.E. (2005). LRP2/megalin is required for patterning of the ventral telencephalon. Development *132*, 405–414.

Tirosh, I., Izar, B., Prakadan, S.M., Wadsworth, M.H., Treacy, D., Trombetta, J.J., Rotem, A., Rodman, C., Lian, C., Murphy, G., et al. (2016). Dissecting the multicellular ecosystem of metastatic melanoma by single-cell RNA-seq. Science *352*, 189–196.

Walker, T.L., and Kempermann, G. (2014). One mouse, two cultures: isolation and culture of adult neural stem cells from the two neurogenic zones of individual mice. J. Vis. Exp. *84*, e51225.

Weigmann, A., Corbeil, D., Hellwig, A., and Huttner, W.B. (1997). Prominin, a novel microvilli-specific polytopic membrane protein of the apical surface of epithelial cells, is targeted to plasmalemmal protrusions of non-epithelial cells. Proc. Natl. Acad. Sci. USA *94*, 12425–12430.

Willnow, T.E., and Christ, A. (2017). Endocytic receptor LRP2/megalin-of holoprosencephaly and renal Fanconi syndrome. Pflugers Arch. *469*, 907–916.

Willnow, T.E., Hilpert, J., Armstrong, S.A., Rohlmann, A., Hammer, R.E., Burns, D.K., and Herz, J. (1996). Defective forebrain development in mice lacking gp330/megalin. Proc. Natl. Acad. Sci. USA *93*, 8460–8464.

Wolf, F.A., Angerer, P., and Theis, F.J. (2018). SCANPY: large-scale single-cell gene expression data analysis. Genome Biol. *19*, 15.

Zarbalis, K., May, S.R., Shen, Y., Ekker, M., Rubenstein, J.L.R., and Peterson, A.S. (2004). A focused and efficient genetic screening strategy in the mouse: identification of mutations that disrupt cortical development. PLoS Biol. *2*, E219.

Zhang, Y., Chen, K., Sloan, S.A., Bennett, M.L., Scholze, A.R., O'Keeffe, S., Phatnani, H.P., Guarnieri, P., Caneda, C., Ruderisch, N., et al. (2014). An RNA-sequencing transcriptome and splicing database of glia, neurons, and vascular cells of the cerebral cortex. J. Neurosci. *34*, 11929–11947.

Zhou, Y., Zhang, X., and Klibanski, A. (2012). MEG3 noncoding RNA: a tumor suppressor. J. Mol. Endocrinol. *48*, R45–R53.

STAR★METHODS

KEY RESOURCES TABLE

REAGENT or RESOURCE	SOURCE	IDENTIFIER
Antibodies		
Rabbit anti-S6-RP	Cell Signaling	Cat#2217S; RRID: AB_331355
Rabbit anti-ID3	Abcam	Cat#Ab41834; RRID: AB_733073
Donkey anti-Rabbit IgG (H+L) Highly Cross-Adsorbed, Alexa Fluor® 488	Invitrogen	Cat#A-20216; RRID: AB_2620928
Rat anti-BrdU	AbD Serotec	Cat#OBT0030; RRID: AB_609569
Donkey anti-rat Biotin SP	Jackson Immuno Research	Cat#712065150; RRID: AB_2340646
Chemicals, Peptides, and Recombinant Proteins		
Percoll	Sigma	Cat#P1644
Droplet generation oil	Bio-Rad	Cat#186-4006
Perfluorooctanol (PFO)	VWR	Cat#SAFA370533-25G
Maxima H Minus RT	Fermentas	Cat#EP0753
Exo I	NEB	Cat#M0293L
Critical Commercial Assays		
Neural tissue dissociation kit (P)	Miltenyi	Cat#130-092-628
2 x KAPA mix	VWR; Roche	Cat#07-KK2601-01; Cat#07958960001
Agencourt AMPure XP beads	Beckman Coulter	Cat#A63881
Nextera XT DNA library preparation kit	Illumina	Cat#FC-131-1096
NextSeq 500/550 High Output kit v2 (75 cycles)	Illumina	Cat#FC-404-2005
ABC-Elite Reagent	Vector Labs	Cat#PK-6100
Tyramide signal amplification	PerkinElmer	Cat#NEL701A001KT
Deposited Data		
Raw and analyzed data	This paper	GEO:GSE111527
Cell cycle gene set	Tirosh et al., 2016	Table S5
Gene annotation (GTF file)	EBI	GRCm38.p4
Mouse genome (FASTA file)	UCSC	mm10
Llorens-Bobadilla cluster gene sets	Llorens-Bobadilla et al., 2015	Table S2
DG gene set	Artegiani et al., 2017	Table S2
Experimental Models: Organisms/Strains		
Mouse: C57BL6/NCrl	Charles River Laboratories	N/A
Mouse: TCF/Lef_LacZ, Lrp2, Lrp2 < 267 >	Spoelgen et al., 2005; Zarbalis et al., 2004; Mohamed et al., 2004	N/A
Oligonucleotides		
Template Switch Oligo AAGCAGTGGTATCAACGCAGAGTGAATrGrGrG	Eurofins	N/A
SMART PCR primer AAGCAGTGGTATCAACGCAGAGT	Eurofins	N/A
New-P5-SMART PCR oligo AATGATACGGCGACCACCGAGATCTACACGCCTGTCCGCGGAAGCAGTG GTATCAACGCAGAGT*A*C *phosphorothioate bond	Eurofins	N/A
N701 CAAGCAGAAGACGGCATACGAGATTCGCCTTAGTCTCGTGGGCTCGGTCGCCTTA	Eurofins	N/A
N702 CAAGCAGAAGACGGCATACGAGATTCGCCTTAGTCTCGTGGGCTCGGCTAGTACG	Eurofins	N/A
N703 CAAGCAGAAGACGGCATACGAGATTCGCCTTAGTCTCGTGGGCTCGGTTCTGCCT	Eurofins	N/A

(*Continued on next page*)

Continued

REAGENT or RESOURCE	SOURCE	IDENTIFIER
N704 CAAGCAGAAGACGGCATACGAGATTCGCCTTA GTCTCGTGGGCTCGGGCTCAGGA	Eurofins	N/A
N706 CAAGCAGAAGACGGCATACGAGATTCGCCTTA GTCTCGTGGGCTCGGCATGCCTA	Eurofins	N/A
N707 CAAGCAGAAGACGGCATACGAGATTCGCCTTAG TCTCGTGGGCTCGGGTAGAGAG	Eurofins	N/A
Custom read 1 primer GCCTGTCCGCGGAAGCAGTGG TATCAACGCAGAGTAC	MWG operon	Cat#4300015339
Software and Algorithms		
Drop-seq tools v1.12	Macosko et al., 2015	http://mccarrolllab.org/dropseq/
Picard-tools v2.9.0	http://broadinstitute.github.io/picard/	http://broadinstitute.github.io/picard/
STAR v2.5.3a	Dobin et al., 2013	https://github.com/alexdobin/STAR
Seurat v1.4	Macosko et al., 2015	https://satijalab.org/seurat/
velocyto v0.11.0	La Manno et al., 2018	http://velocyto.org/velocyto.py/
EdgeR v3.22.3	Robinson et al., 2010	R Bioconductor
lme4 v1.1	Bates et al., 2015	R Bioconductor
SCANPY v1.2.2	Wolf et al., 2018	https://github.com/theislab/scanpy
Other		
SVZ dissection	Walker and Kempermann, 2014	N/A
3-density percoll gradient	Guez-Barber et al., 2012	N/A
Methanol fixation	Alles et al., 2017	N/A
Drop-seq	Macosko et al., 2015; Alles et al., 2017	N/A
Microfluidic polydimethylsiloxane (PDMS) co-flow device	FlowJEM	Cat#4400023716
Fine-bore polyethylene tubing	Smiths Medical	Cat#800/100/120
Syringe pumps Legato 100	KD Scientific	Cat#78-8100
Barcoded BeadsSeqB	ChemGenes	Cat#MACOSKO-2011-10
Magnetic stir disc	VP scientific	Cat#VP772DP-N42-5-2
Rotary magnetic stirrer	VP scientific	Cat#VP710D2CE/VP71D2-4
Resource web site (SVZ Cell Atlas)	This paper	https://shiny.mdc-berlin.de/SVZapp/

CONTACT FOR REAGENT AND RESOURCE SHARING

Further information and requests for resources and reagents should be directed to and will be fulfilled by the Lead Contact, Nikolaus Rajewsky (rajewsky@mdc-berlin.de).

EXPERIMENTAL MODEL AND SUBJECT DETAILS

Animals

Experiments involving animals were performed according to institutional guidelines following approval by local authorities (X9017/12). Mice were housed in a 12 hour light-dark cycle with *ad libitum* food and water. We used adult mice (2-4 month of age) for our experiments. All mice used in this study were healthy and immune-competent, and did not undergo previous procedures unrelated to the experiment. For dataset A of the Drop-seq experiments (experiment identifiers an002, an003F, an003L, an008, and an009), we used female and male C57BL6/N mice (overview in Figure S1A). For immonstainings and Drop-seq experiments with the identifiers an007 and an0010 (dataset B), we used male LRP2-deficient mice (KO) and matched littermate controls (Ctrs) (overview in Figure S5A). KO mice were compound heterozygous for two different *LRP2 null* alleles. One allele ($LRP2^{+/-}$) was derived by targeted gene disruption (Spoelgen et al., 2005). This line was crossed with the *Tcf/Lef_LacZ* reporter strain (Mohamed et al., 2004). The second mutant allele ($Lrp2^{267/+}$) was derived in an ENU mutagenesis screen (Zarbalis et al., 2004). LRP2 KO animals *(Tcf/Lef_LacZ, $Lrp2^{267/-}$)* were derived from F1 crosses of (*Tcf/Lef_LacZ, $Lrp^{+/-}$*) and $Lrp2^{267/+}$ animals. As no obvious phenotypes were observed in mice carrying only one targeted *Lrp2* allele, both heterozygous and wild-type animals were used as controls (referred to as Ctr throughout the study). Drop-seq samples an007_KO and an010_KO were derived from three and four LRP2-deficient mice (KO), respectively. Samples with the identifiers an007_WT and an010_WT were derived from wild-type and heterozygous littermate

controls: an007_WT contained cells derived from one wild-type and three heterozygous mice; for an010_WT, two wild-type and two heterozygous mice were used.

METHOD DETAILS

Generation of SVZ single-cell suspension

For each Drop-seq experiment, three to five mice were deeply anesthetized by intraperitoneal injection of pentobarbital (100 μl of 160 mg/mL pentobarbital sodium solution per mouse) and subsequently transcardially perfused with 20-25 mL ice cold NaCl/Heparin solution (40 μl Heparin-Natrium (250,000 I. E./10 mL) in 500 mL 0.9% NaCl) until the liver was pale. Brains were immediately extracted and collected in ice cold Hanks' Balanced Salt Solution (HBSS) without Ca^{2+} and Mg^{2+} (Sigma-Aldrich #55021C). The SVZ of the lateral ventricles was microdissected as described in Walker and Kempermann (2014). SVZs from up to five brains were pooled for one enzymatic dissociation reaction using the Neural Tissue Dissociation Kit (P) (Miltenyi #130-092-628) with minor changes: for enzyme mix 1, 1900 μl buffer X was supplemented with 0.96 μl 0.143 M beta-mercaptoethanol (final concentration 70 μM) and 7.8 μl 10% bovine serum albumin (BSA; final concentration 0.04%; molecular biology grade) one day in advance and stored at 4°C. Fifty μl enzyme P was added briefly before use and the enzyme mix was pre-warmed to 37°C. SVZ tissue was slightly minced on ice and transferred into a 15 mL tube using the pre-warmed enzyme mix and a P1000 pipette with the tip cut in front. After 15 minutes incubation at 37°C (slowly rotating), enzyme mix 2 was added and the tissue carefully dissociated by pipetting ten times up and down with a P1000 pipette. The suspension was incubated another 10 minutes at 37°C (slowly rotating) and dissociated again by careful pipetting as before. In cases of remaining tissue clumps, a P200 pipette tip was placed in front of the P1000 tip and few additional, very careful pipetting steps were added. Subsequently, the enzymatic digestion was stopped by adding 5 mL room temperature HHB solution (HBSS with Ca^{2+} and Mg^{2+} (Sigma-Aldrich #55037C), 10 mM HEPES, 0.01% BSA). Cells were filtered through a 70 μm cell strainer (Sigma #CLS431751-50EA; pre-wet with 1 mL HHB). The previous cell tube and the filter were washed twice with 1 mL HHB. After centrifugation for 10 minutes at 10°C and 350xg, cells were resuspended in HHB for the following 3-density centrifugation step to remove small cellular debris (based on Guez-Barber et al., 2012, in the following referred to as percoll gradient). If tissue from four to five mice was used, three percoll gradients (in three 15 mL tubes) were processed in parallel and cells were resuspended in 3 mL HHB (tissue from 2-3 mice was resuspended in 2 mL HHB for two individual percoll gradients). To form the 3-density gradient, 1 mL of each ice cold solution (high density: 19% percoll (Sigma #P1644), 22.5 mM NaCl in HBSS/HEPES (HBSS with Ca^{2+} and Mg^{2+}, 10 mM HEPES); medium density: 15% percoll, 17.7 mM NaCl in HBSS/HEPES; low density: 11% percoll, 13.8 mM NaCl in HBSS/HEPES) were carefully layered on top of each other in a 15 mL Falcon tube on ice starting with the high density solution at the bottom. Last, 1 mL of the filtered cell suspension was applied on top. After 3 minutes centrifugation at 430xg and 4°C, the cloudy top layer containing debris and dead cells was removed and discarded (about 2 mL per tube). Subsequently, cells were pelleted by 5 minutes centrifugation at 550xg and 4°C, resuspended in ice cold PBS/0.01% BSA, pooled and filtered through a pre-wet 20 or 30 μm strainer (20 μm: HiSS Diagnostics #43-50020-03, 30 μm: Miltenyi #130-041-407). Remaining tubes and strainer were washed twice with 0.1 mL PBS/0.01% BSA. Finally, cells were counted using trypan blue (Sigma # T8154) in a Neubauer counting chamber and either diluted to 100 cells/μl using PBS/0.01% BSA (proceed with Drop-seq directly), or fixed in methanol as described below for later use.

Fixation and rehydration of cells for Drop-seq

In two out of nine Drop-seq experiments, living, single-cells were fixed in methanol and therefore preserved for later experiments (according to Alles et al., 2017). In short, the final single-cell suspension was centrifuged for 5 minutes at 300xg and 4°C to reduce the volume to 200 μl. The single-cell suspension was vortexed gently and 800 μl 100%, −20°C cold methanol was added dropwise to reach a final methanol concentration of 80%. After 15 minutes incubation on ice, the cell suspension was transferred to a 1.5 mL Eppendorf tube, sealed with Parafilm and stored at −20°C or −80°C until use. For Drop-seq, cells were equilibrated on ice for 5-10 minutes and subsequently centrifuged for 10 minutes at 500xg and 4°C. The supernatant was discarded, and cells resuspended in 0.5 mL rehydration solution (PBS, 0.01% BSA, 1:40 RiboLock; Fisher Scientific #EO0382). Cells were filtered through a 30 μm filter and diluted to either 50 cells/μl (experiment an003F) or 100 cells/μl (experiment an002) with rehydration solution. The cell recovery rate was about 50%.

Drop-seq run

Drop-seq was performed as described in Alles et al. (2017), based on Macosko et al. (2015) and the Drop-seq laboratory protocol version 3.1 (12/28/15), Evan Macosko and Melissa Goldman, Steve McCarroll's lab, Harvard Medical School. In detail, monodisperse droplets with a volume of about 1 nL were generated using a self-built Drop-seq setup: a microfluidic polydimethylsiloxane (PDMS) co-flow device (FlowJEM #4400023716; rendered hydrophobic by pre-treatment with Aquapel) was placed on the stage of a light sheet microscope. Tubing (fine-bore polyethylene tubing, Smiths Medical #800/100/120) connected the device to three syringes placed in syringe pumps (KD Scientific, Legato 100 #78-8100) and a 50 mL Falcon tube serving as outflow container. One end of tubing was stuck directly into the device, the other end connected to the syringe via a 26G needle (Sigma-Aldrich #Z192392-100EA). The first syringe (20 mL, BD Plastikpak #300629) contained droplet generation oil (Bio-Rad #186-4006). The second syringe (3 mL, BD #309657) was used for the single-cell suspension. For the third syringe (3 mL) the barcoded microparticle suspension

(Barcoded Beads SeqB, ChemGenes, #MACOSKO-2011-10) was prepared as follows: aliquots containing approximately 180,000 barcoded beads were stored in TE-TW (10 mM Tris pH 8.0, 1 mM EDTA, 0.01% Tween-20). Shortly before use, beads were pelleted by centrifugation and the TE-TW was removed. After resuspension in 1.5 mL lysis buffer (6% Ficoll PM-400 (GE Healthcare, #GE17-0300-10), 6% sarkosyl (Sigma #L5125-100G), 20 mM EDTA, 200 mM Tris pH 7.5, 50 mM DTT), the bead suspension (120 beads/μl) was loaded into the 3 mL syringe containing a magnetic stir disc (VP scientific #VP772DP-N42-5-2). The syringe was placed in a vertical orientated syringe pump. A rotary magnetic stirrer (VP scientific #VP710D2CE/VP71D2-4) was set to a speed of 25-30 to provide constant mixing of beads. The syringe containing beads in lysis buffer was connected at last to the device to circumvent contact of cells with lysis buffer. For one Drop-seq run aiming for 1,000-2,000 single-cell transcriptomes at a cell input concentration of 100 cells/μl, approximately 7 mL oil, 1.5 mL cell and 1.5 mL bead suspension were needed. When everything was connected, syringe pumps were started in the following order: first cell, next bead, and last oil pump at flow rates of 4,000 μl/hour for cells and beads, and 15,000 μl/hour for oil. Droplet formation was monitored under the microscope. As soon as droplets were formed uniformly and continuously, the waste tube was replaced with a new 50 mL tube and droplets were collected for 12.5 minutes (corresponds to the collection of approximately 100.000 beads). Immediately after collection, droplets were broken and library preparation was started.

Assessment of droplet quality

The quality of droplets was evaluated by bright field microscopy. Therefore, 17 μl droplet generation oil was placed into a Fuchs-Rosenthal hemocytometer chamber (NanoEnTek #DHC-F01) and gently mixed with 3 μl of the collected droplet emulsion by rocking the chamber back and forth few times. The prepared chamber was kept on ice and imaged when the single-cell library preparation was at the reverse transcription step. Usually, droplets were uniform in size and less than 5% of bead occupied droplets contained two beads.

Droplet Breakage

At the end of the collection time, the collection tube was replaced with the waste tube and the run was ended by stopping first the bead, next the cell, and last the oil pump. In the collection tube, two phases were visible: the upper layer was formed by the droplet emulsion, the lower layer by excessive oil. First, the oil was removed carefully using a P1000 pipette (2-3 mL). Next, 30 mL room temperature 6xSSC (Sigma #S6639-1L) and 1 mL perfluorooctanol (PFO, VWR #SAFA370533-25G) were added. Droplets were broken by three to four forceful vertical shakes. Samples were kept on ice during the breakage protocol to reduce the likelihood of annealed RNAs to dissociate from the beads. After centrifugation at 1000xg for 1 minute in a swing bucket centrifuge (brakes set to 7), beads floated on the interface. The supernatant on top of beads was removed carefully. Thirty mL 6xSSC were used to kick up the beads into solution. As the oil was heavier than the beads, it fell quickly to the bottom of the tube while beads were still floating. Beads in suspension were pipetted in a fresh 50 mL tube and centrifuged for 1 minute at 1000xg. After removing the supernatant, beads were transferred from the bottom of the 50 mL tube into a 1.5 mL Eppendorf tube. Beads were washed twice with 1 mL 6xSSC and pelleted using a tabletop centrifuge. Finally, beads were resuspended in 300 μl self-made 5xreverse transcriptase (RT) buffer (250 mM Tris pH 8.0, 375 mM KCl, 15 mM MgCl2, 50 mM DTT).

Single-cell library generation and sequencing

Beads in 5xRT buffer were centrifuged for 1 minute at 1000xg. After removing as much of the 5xRT buffer as possible, beads were resuspended in 200 μl RT mix (1x Maxima RT buffer, 2,000 U Maxima H Minus RT (Fermentas #EP0753), 4% Ficoll PM-400 (GE Healthcare # GE17-0300-10), 1 mM dNTPs (Fermentas #R0152), 5 μl RNase inhibitor (Lucigen #30281-1-LU), 1.25 μM Template Switch Oligo (Eurofins, sequence in the Key Resources Table). The sample was incubated with rotation (neoLab Rotator with Vortex RM-2M #7-0045, program F5 RPM12) first for 30 minutes at room temperature and subsequently for 90 minutes at 42°C. Reverse transcription was stopped by washing the beads once with 1 mL TE-SDS (10 mM Tris pH 8.0, 1 mM EDTA, 0.5% SDS) and twice with 1 mL TE-TW (10 mM Tris pH 8.0, 1 mM EDTA, 0.01% Tween-20). Before starting the Exonuclease I (Exo I) treatment to digest bead primers which did not capture an RNA molecule, beads were washed once more with 1 mL 10 mM Tris pH 8.0. Afterward, beads were resuspended in 200 μl Exo I mix (1x Exo I buffer, 200 U Exo I, NEB #M0293L) and incubated at 37°C for 45 minutes with rotation (neoLab Rotator with Vortex RM-2M #7-0045, program F5 RPM12). Beads were washed once with 1 mL TE-SDS, twice with 1 mL TE-TW and before proceeding with PCR once more with 1 mL water. After the last washing step, beads were resuspended in 1300 μl PCR mix (0.8 μM SMART PCR primer (Eurofins, sequence in the Key Resources Table), 650 μl 2x KAPA mix (either VWR # 07-KK2601-01 or Roche #07958960001)). Beads were mixed well and aliquoted in 25 PCR tubes (50 μl per tube). PCR was performed in a thermocycler with the following protocol: 95°C 3 minutes; four cycles of: 98°C 20 s, 65°C 45 s, 72°C 3 minutes; nine cycles of: 98°C 20 s, 67°C 20 s, 72°C 3 minutes; final extension step at 72°C for 5 minutes. After PCR, 20 μl from each PCR tube were pooled together (resulting in 500 μl PCR product) and purified with Agencourt AMPure XP beads (Beckman Coulter #A63881) according to the manufacturer's instructions using a 0.6x AMPure XP beads to sample ratio. The sample was eluted in 80 μl water and purified once more. Finally, the sample was eluted in 11 μl water. One μl of the SMART library was evaluated by running a BioAnalyzer High Sensitivity Chip (Agilent #5067-4627) according to the manufacturer's instructions. The average size of the library was usually 1,300 – 2,000 bp. To tagment the library with the Nextera XT DNA library preparation kit (Illumina #FC-131-1096) using custom primers that amplify only the 3′ends, 600 pg of the SMART PCR sample in 5 μl water were mixed in a PCR tube with 10 μl Nextera

Tagmentation DNA buffer and 5 μl Amplicon Tagmentation Mix by pipetting up and down 5 times. After spinning down, the sample was incubated in a preheated thermocycler at 55°C for 5 minutes and subsequently put on ice. The sample was neutralized by adding 5 μl of NT buffer and pipetting up and down 5 times. Samples were spun down and incubated at room temperature for 5 minutes. For PCR, reagents were added in the following order: 15 μl Nextera PCR mix (NPM), 8 μl water, 1 μl 10 μM New-P5-SMART PCR hybrid oligo (Eurofins, sequence in the Key Resources Table), 1 μl of 10 μM Nextera Index primer N70X. Nextera index primers were used for sample identification after sequencing as four Drop-seq samples were multiplexed in one flowcell. Here, the primers N701, N702, N703, N704, N706 and N707 (Eurofins, sequences in the Key Resources Table) were used in combinations with greatest hamming distances. Amplification was performed in a thermocycler using the following protocol: 95°C 30 s; twelve cycles of: 95°C 10 s, 55°C 30 s, 72°C 30 s; final extension step 72°C 5 minutes. The final library was purified with Agencourt AMPure XP beads according to the manufacturer's instructions using a 0.6x AMPure XP beads to sample ratio. The library was eluted in 20 μl water and purified again but this time using a 1.0x AMPure XP beads to sample ratio. Finally, the library was eluted in 11 μl water and evaluated by running a BioAnalyzer High Sensitivity Chip and measuring the concentration with the Qubit fluorometer (dsDNA HS Assay Kit, Invitrogen #Q32854). Libraries had an average size of 500-850 bp and concentrations varying between 0.3 and 2.6 ng/μl.

For sequencing with the NextSeq 500/550 High Output kit v2 (75 cycles, Illumina #FC-404-2005) on Illumina NextSeq500 sequencers, four Drop-seq libraries were pooled at equal molarities, diluted and denatured following the manufacturer's instructions. Final libraries had a concentration of 1.8 pM and contained 1% PhiX spike-in for run quality control. Sequencing was performed in paired-end mode. For priming read 1, custom read 1 primer was provided (MWG operon #4300015339, sequence in the Key Resources Table). Read 1 was set to 20 bp to cover the cell barcode (bases 1-12) and the UMI (bases 13-20). Read 2 was 64 bp long and used to identify the transcript. The index read, which is needed for demultiplexing, was set to 8 bp.

BrdU labeling experiments

To label proliferating cells in the adult mouse brain, animals were injected intraperitoneal once with BrdU (50 mg/kg body weight) and sacrificed 24 hours later by intraperitoneal injection of pentobarbital (as before) followed by transcardial perfusion with 4% paraformaldehyd (PFA). Brains were collected and processed for routine paraffin embedding and sectioning. Ten μm sections were washed with 2.4% H_2O_2 in 1xTBS for 30 minutes, treated with 2 N HCl at 45°C for 1.5 hours, and neutralized by washing in 0.1 M borate buffer (pH 8.5) for 15 minutes at room temperature. Sections were blocked in 10% donkey serum in 1xTBS/0.3% Triton X-100 for 1 hour, and subsequently incubated with rat anti-BrdU antibody (1:500; AbD Serotec #OBT0030) overnight at 4°C, followed by donkey anti-rat Biotin SP antibody (1:250; Jackson Immuno Research #712065150) for 2 hours, and finally 1 hour in ABC-Elite Reagent (Vector Labs #PK-6100). The color reaction was performed using Ni-diamino benzidine.

Immunohistology

Standard immunohistology was performed on free-floating sections. Therefore, PFA fixed brains were infiltrated with 30% sucrose in PBS for 48 hours, cut into 40 μm sections, and stored in cryoprotectant (25% Glycerol, 25% Ethylene Glycol, 50% Phosphate Buffer pH 7.8) at −20°C until further use. Tissue sections were incubated with primary antibodies at the following dilutions: rabbit anti-S6-RP (1:50; Cell Signaling #2217S) or rabbit anti-ID3 (1:100; Abcam #Ab41834). Bound primary antibody was visualized using donkey anti-Rabbit antisera conjugated with Alexa 488 (1:500; Invitrogen #A-20216) for S6-RP or the tyramide signal amplification kit (PerkinElmer #NEL701A001KT) for ID3. Pictures were taken on a confocal SPE microscope. We counted individual ID3 positive cells and quantified the mean gray value for S6-RP in the SVZ using the software ImageJ.

LacZ staining

For LacZ staining, dissected brains were fixed for 3 hours in 4% PFA and infiltrated with 30% sucrose in PBS for 48 hours. Tissues were embedded in Tissue-Tek OCT (Sakura, Japan), cooled down on dry ice, sectioned at 12 μm thickness on a rotary cryotome (Leica, Germany), and stored at −20°C until further use. To start the staining procedure, slides were thawed for 5 minutes at room temperature and sections subsequently fixed by incubation in 1xPBS (pH 7.4), 2 mM $MgCl_2$, 5 mM EGTA, 0.2% Glutaraldehyd for 5 minutes. Following washing steps with 1xPBS plus 2 mM $MgCl_2$, sections were permeabilized with 1xPBS, 0.02% NP40, 0.01% Sodium Deoxycholate, 2 mM $MgCl_2$ for 10 minutes, and incubated overnight at 37°C in 1 mg/mL X-GAL (5-Bromo-4Chloro-3-indolyl-B-D-galactopyranoside) solved in staining solution (1xPBS, 20 mM Tris (pH 7.3), 0.02% NP40, 0.01% Sodium Deoxycholate, 2 mM $MgCl_2$, 5 mM Potassium Ferrocyanide). Images were acquired on a bright field microscope (Olympus BX51TF).

QUANTIFICATION AND STATISTICAL ANALYSIS

Definition of significance

The term significant was used, if the p value of a result was smaller than 0.05. Exact p values are reported in the figures, figure legends, supplementary tables, and according methods.

Drop-seq computational pipeline: Data processing, alignment and gene quantification

Sequencing quality was assessed by FastQC. To produce the digital gene expression matrix (DGE), we used the Drop-seq tools v1.12 and Picard-tools v2.9.0, following the standard pipeline in the Drop-seq core computational protocol v1.2 with default

parameters (based on Macosko et al., 2015). In brief: We extracted the UMIs and cell barcodes from read 1 before discarding it, added them as metadata information (tags) to the corresponding sequence of read 2, and performed the downstream analysis as in single-end mode. Reads with low quality barcodes were discarded. We trimmed potential SMART adaptor contaminants and poly(A) stretches. Subsequently, reads were aligned to the mouse genome mm10 using STAR v2.5.3a with default parameters (Dobin et al., 2013) and annotated according to GRC38m.p4. Typically, 60%–80% of reads mapped uniquely to the genome. Non-uniquely mapped reads were discarded. We corrected reads for bead synthesis errors such as missing last base of the cell barcode. For each sample, the number of cells was estimated by plotting the cumulative distribution of reads per cell against the barcodes sorted by descending number of reads and calculating the inflection point ("knee"). The inflection point was calculated considering the top 25,000 barcodes for all samples except an007_KO and an007_WT for which the top 15,000 barcodes were considered. Finally, we extracted the DGE for each sample.

Cell and gene filtering

For downstream analysis, we excluded cells which expressed less than 500 UMIs, less than 200 genes, or had more than 10% of total UMIs quantified from mitochondrial genes. Furthermore, we removed genes which were expressed in less than three cells. All samples were analyzed as described in the next paragraph. After individual analysis and comparison of replicates, DGEs from replicates were combined. For dataset A, the DGEs of five independent Drop-seq runs were pooled. We excluded 91 cells, which formed four small cell clusters consisting of one to three replicates only. After filtering, dataset A comprised 9,804 cells, which were analyzed further. In dataset B, the DGEs of four Drop-seq runs (two replicates with LRP2-knockout and littermate Ctr derived cells processed in parallel) were pooled resulting in 8,056 cells for further analysis.

Normalization, clustering, marker discovery, and data visualization

The following analysis was performed using Seurat v1.4. To normalize UMI counts for every gene per cell, we divided its UMI counts by the total number of UMIs in that cell, multiplied the value by 10,000 and applied a logarithmic transformation. To calculate the Pearson correlation of gene expression between single-cell samples (Figure S1B), the normalized UMI expression of each sample was averaged per gene and then samples were compared with each other. The scatterplot was produced with R plotting.

For clustering, we used the MeanVarPlot function to select genes with most variation across cells, an average expression between 0.01 and 3 normalized UMI counts, and a minimum standard deviation of 1. With these genes we performed principal component analysis (PCA) to further reduce the dimensions of the data. By applying the jackstraw function, we identified the principal components with a p=value smaller than 0.01, which were used for further analysis. We used this PCA transformation to perform clustering with SNN-cliq. We evaluated which resolution parameter is appropriate by testing several different parameters in combination with the AssesNode function. The resolution parameter determines in how much detail cells are partitioned into clusters, whereas the AssessNode function merges clusters, which are not meaningful. In the end, dataset A was clustered with a resolution of 1.0 and dataset B with 0.8, respectively. Dendrograms representing cluster relationships were produced with the BuildClusterTree function. For data visualization, we performed t-distributed stochastic neighbor embedding (tSNE). To identify cell type enriched genes, we applied the FindAllMarkers function with the parameters min.pct and thresh.use set to 0.25. To identify significantly up- and downregulated genes in NSCs compared to astrocytes, we used the FindMarkers function. The results were visualized in heatmaps produced with the DoHeatmap function. The expression of single genes was depicted using custom R scripts, either per cell cluster as distribution of normalized UMI counts (violins) or per cell as color gradient in tSNE space. In Figure S4F, we added a random number drawn from a normal distribution (mean 0 and standard deviation 1) and divided by 100 to the normalized UMI counts. Adding "noise" reduces the background and therefore improves the visualization of gene expression per cell type.

RNA velocity analysis

To calculate the RNA velocity, we applied the velocyto python package (La Manno et al., 2018). Velocyto counts the spliced and unspliced reads separately. After normalization, variable gene selection, and smoothing/imputation, the method uses all cells to estimate the expected steady state ratio between spliced and unspliced molecules. From here, velocyto calculates and assigns an RNA velocity value for each gene per cell to extrapolate the future transcriptional cell state. We run the command line interface (CLI) of velocyto (version 0.11.0) in permissive mode. Using all cells from dataset A, we normalized, selected the top 1,000 variable genes further thresholding for minimum expression, performed data imputation with a neighborhood of 200 cells, and calculated the RNA velocities. All steps were performed following the built-in functions. We then isolated astrocytes, NSCs, TAPs and NBs based on the clustering by Seurat (as described above) and plotted their RNA velocities in tSNE space. Finally, we estimated the differentiation starting point of the selected cells by using the backward Markov process on the transition probability matrix to determine high density regions. All steps were performed with default parameters.

Subclustering

To produce the subclusterings of dataset A and dataset B, cells belonging to the clusters of interest were isolated from the DGE and the Seurat analysis was repeated with the clustering resolution set to 0.8 and 0.7, respectively.

Diffusion pseudotime analysis

Pseudotime of the neurogenic lineage (dataset A, subclusters 3-8) was calculated according to Haghverdi et al. (2016) and reimplemented in SCANPY (Wolf et al., 2018) with default parameters and zero branchings. As starting point, a random cell from the qNSC cluster was selected. The determined pseudotime was plotted in tSNE space and used to order the cells. To visualize gene expression along pseudotime, we applied local regression (loess) with degree of smoothing $\alpha = 20\%$ on the normalized UMI counts to get a smooth line. Finally, the values for each gene were scaled to (0, 1) range by dividing with the maximum value of the loess prediction.

Gene set scoring

For cell type characterization and comparison of our data with the literature, we downloaded previously published gene sets (Llorens-Bobadilla et al., 2015) and scored our cells as follows: Genes, which were not in the gene sets or had an expression of less than 50 UMIs across all cells of interest were discarded from the normalized DGE. The expression range of remaining genes was linearly transformed to (0, 1) range for every gene. The score per cell was calculated by averaging the transformed gene expression values of all genes from a certain gene set. The distribution of scored cells was plotted as violin per subcluster and gene set.

Comparison gene expression profiles

To compare gene expression profiles of SVZ and DG cell types, we took a published gene list, which contains per cell type the mean and variance of differentially expressed genes between DG cell types (Artegiani et al., 2017, Table S2, 4,595 genes), and built the intersect with all genes identified to be differential between SVZ cell types (this study, Table S1, 3,945 genes). After averaging the expression of each gene in the intersect gene list (2,438 genes) for all SVZ clusters, we calculated the Pearson correlation for all SVZ and DG clusters and visualized the results in a heatmap.

Proliferation analysis of cells derived from LRP2-deficient versus Ctr SVZ (dataset B)

Following the method above (gene set scoring), we scored all cells from dataset B according to cell cycle using a published gene set (Tirosh et al., 2016). Per cell cluster and condition (LRP2 KO versus Ctr), we calculated the cumulative fraction of cells against the score. We performed Kolmogorov-Smirnov test comparing the cumulative distributions of the two conditions for each cluster to determine statistical significance of data.

Differential gene expression analysis of cells derived from LRP2-deficient versus Ctr SVZ

To identify genes, which are deregulated in cells derived from LRP2-deficient as compared to Ctr SVZ, we performed differential gene expression analysis (DE) in each cell cluster using edgeR (Robinson et al., 2010). We analyzed both replicates independently (an007_WT versus an007_KO and an010_WT versus an010_KO). Each cell was considered as a sample. We compared the gene expression of cells belonging to the same cluster between conditions (LRP2 KO versus Ctr). As normalizing factor, we used the total UMIs of each cell. Here, we report only genes, which had a p value smaller than 0.01 and a fold change into the same direction in both replicates (an007 and an010). Data was visualized using MA plots: y axis represents the log2 ratio between the averages of a genes expression in KO versus Ctr derived cells (log2FC), x axis represents the log2 average UMI expression over Ctr cells. To all averages a pseudocount of 1 was added.

Ribosomal gene expression comparison of cells derived from LRP2-deficient versus Ctr SVZ

We compared the expression of ribosomal protein genes versus the expression of remaining genes in cells derived from LRP-deficient versus Ctr SVZ. First, we discarded genes with an average expression lower than 0.5 log2 (mean normalized UMI counts) in Ctr cells. Second, we separated ribosomal genes and all remaining genes. We calculate the log2FC, as described in the MA-plot paragraph. The distributions of the two gene sets were plotted separately for each cluster as violin plots. Statistical significance of data was determined using unpaired Student's t test.

Generalized linear mixed model

To test whether cluster proportions change due to genotype (LRP2 KO or Ctr), we employed a generalized linear mixed model (GLMM) with a binomial distribution. The GLMM can estimate the effects of each factor (e.g., condition or batch) on cell type proportions. We modeled the condition as a fixed and the batch as a random effect. We used a binomial distribution because the response for every cell is binary (meaning every cell either belongs to the given cluster or not). We employed a Laplace approximation to estimate the parameters of the model, using the glmer function of the lme4 package in R (Bates et al., 2015).

Statistical analysis of immunohistochemistry data

Statistical details of experiments can be found in the figure legends. Depicted are mean values ± standard error of the mean (SEM). Statistical significance of data was determined using unpaired Students's t test. n represents the number of evaluated animals. In the BrdU experiment, twelve sections from each animal, five animals per genotype (ten mice total) were evaluated. In the ID3 experiment, three sections each from five LRP2-deficient and six control mice (eleven mice total) were analyzed. In the S6-RP experiment, the mean fluorescence intensity was measured per vSVZ section. Three sections from four animals per genotype (eight mice total) were evaluated.

DATA AND SOFTWARE AVAILABILITY

The accession number for the sequencing data reported in this paper is GEO: GSE111527.

ADDITIONAL RESOURCES

The SVZ cell atlas (dataset A) is publicly available in an interactive online tool: https://shiny.mdc-berlin.de/SVZapp/. In the first tab (All Cells) the expression of individual genes can be explored and visualized in 9,804 single cells derived from the adult SVZ. The second tab (Neurogenic Lineage) contains the subclustering analysis of NSCs, TAPs, and NBs and provides higher resolution of the neurogenic lineage.

Cell Reports, Volume *25*

Supplemental Information

Single-Cell Transcriptomics Characterizes Cell Types in the Subventricular Zone and Uncovers Molecular Defects Impairing Adult Neurogenesis

Vera Zywitza, Aristotelis Misios, Lena Bunatyan, Thomas E. Willnow, and Nikolaus Rajewsky

A

exp_ID	fixation	sex	# animals	age (weeks)	# cells	median UMIs/cell	median genes/cell
an002	MeOH	f	5	16.7	1788	1141	713.5
an003F	MeOH	f	5	13.7	855	1410	859
an003L	-	f	5	13.9	2362	1720	1024
an008	-	m	4	13.1	2994	924.5	625
an009	-	mix	2 f, 2 m	13.4	1805	938	624

B

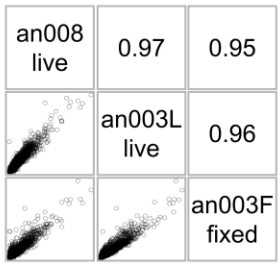

C

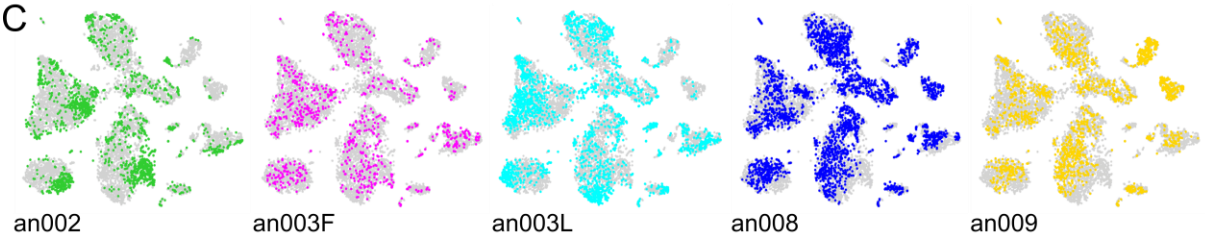

D

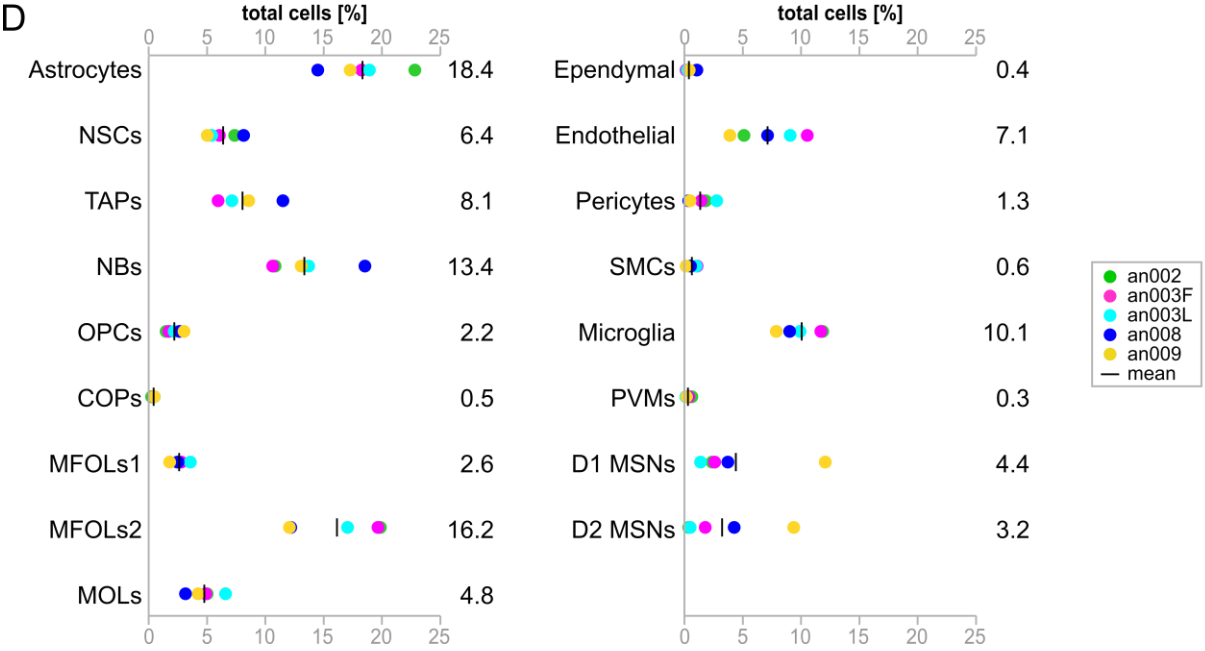

Figure S1. Cluster composition and distribution of replicates across cell types. Related to Figure 2.

(A) Overview of replicates.

(B) Gene expression levels from live and fixed cells correlate well. Upper right panels show Pearson correlation. Lower left panels show pairwise correlation of genes (averaged normalized UMI counts).

(C) Distribution of replicates in the all-cell tSNE plot. Cells from one replicate are colored and plotted on top of all other cells (in gray).

(D) Proportions of cell types. Numbers represent the mean.

Abbreviations: exp_ID: experiment identifier; MeOH: methanol; f: female; m: male; UMIs: unique molecular identifiers. Cell type abbreviations as in Figure 2.

Figure S2. Marker gene expression. Related to Figure 2.

tSNE plots of 9,804 cells colored by the expression of certain marker genes (yellow indicates low, red indicates high expression): *Gja1*: astrocytes and NSCs; *Egfr*: activated NSCs and neural progeny; *Pcna*: proliferating cells; *Foxj1, Ak7*: ependymal cells; *Dlx1, Dlx2*: committed neural progenitors; *Tubb3*: neuroblasts; *Rbfox3, Snap25*: mature neurons; *Tac1*: D1 MSNs; *Penk*: D2 MSNs; *Cx3cr1*: microglia; *C1qa*: immune cells (microglia and PVMs);

Lyz2: PVMs; *Acta2*: SMCs and ependymal cells; *Vtn*: pericytes; *Cspg4*: pericytes and OPCs; *Pdgfra, Olig2*: OPCs; *Olig1*: oligodendrocytes; *Fyn, Bmp4*: COPs; *Opalin, Mal*: MFOLs; *Klk6*: MOLs. *Bfsp2* is a putative new marker gene to discriminate MFOLs1 from MFOLs2. *Bfsp2* was highest expressed in MFOLs1, but also detected in COPs (green circle) indicating that MFOLs1 represent an earlier stage of myelin-forming oligodendrocytes than MFOLs2. Classification of oligodendrocyte clusters was based mainly on genes published in Marques et al. (2016). Squares are close ups of certain cell clusters. Red circles enclose putative ChAT neurons. At the bottom right: tSNE colored by cluster annotation.
Cell type abbreviations as in Figure 2.

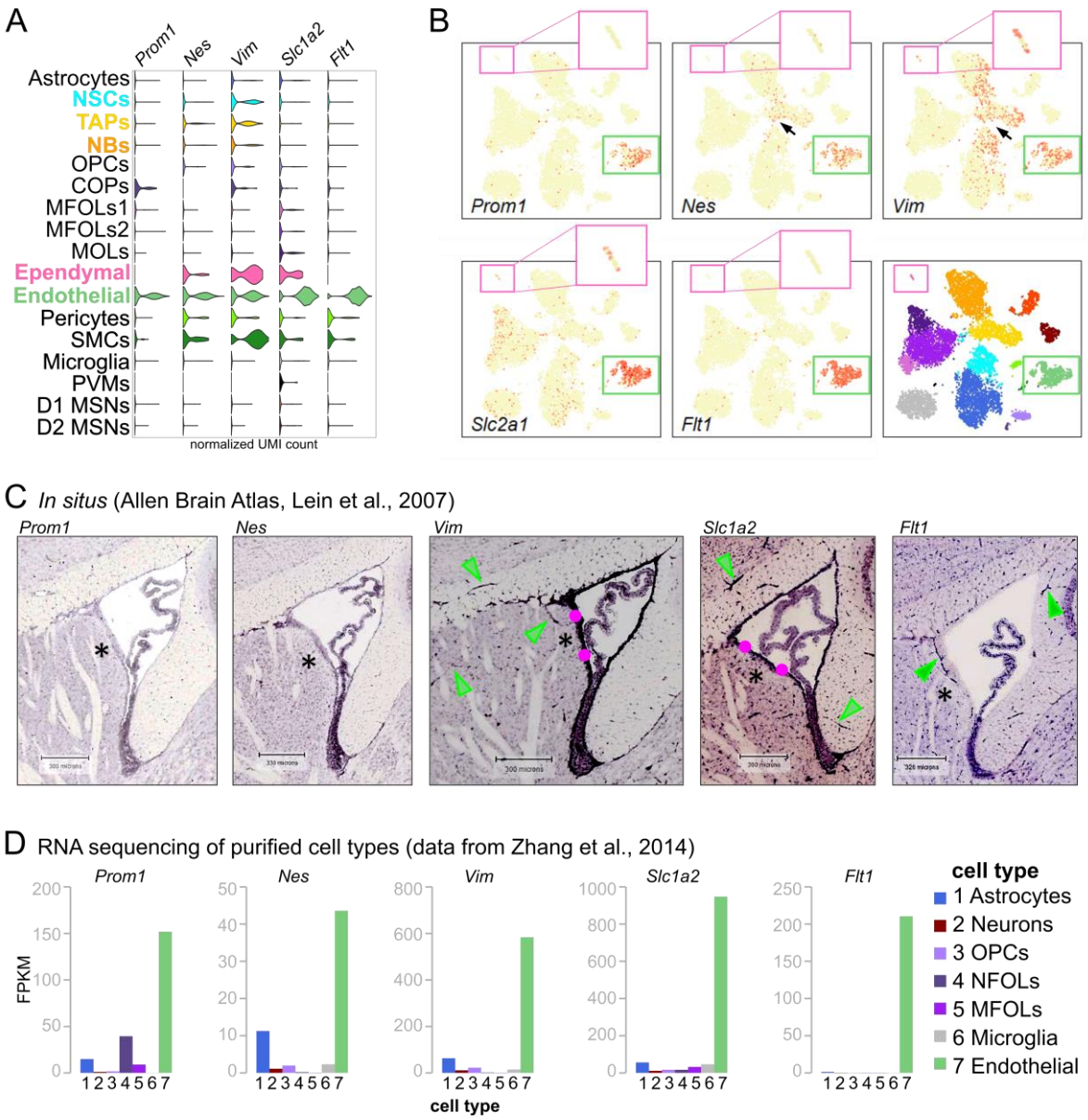

Figure S3. Characterization of endothelial cells. Related to Figure 2.

(A, B) Expression of genes associated with ependymal, endothelial, neural stem and progenitor cells.

(B) Pink boxes highlight and zoom into the ependymal cell cluster. Endothelial cells are highlighted by green boxes. Arrows point at neural progenitors. Yellow indicates low, red indicates high expression. At the bottom right: tSNE colored by cluster annotation.

(C) *In situ* images from the Allen Brain Atlas (Lein et al., 2007) depicting the expression of genes from A and B in the adult mouse brain. *Prom1* and *Nes* mRNA was barely detected. Green arrowheads point to blood vessels. Pink circles highlight staining of the ependymal cell layer. Asterisks label the lateral wall.

(D) Expression of genes from A-C in published bulk RNA sequencing data from sorted cell populations (data from Zhang et al., 2014).

Abbreviations as in Figure 2.

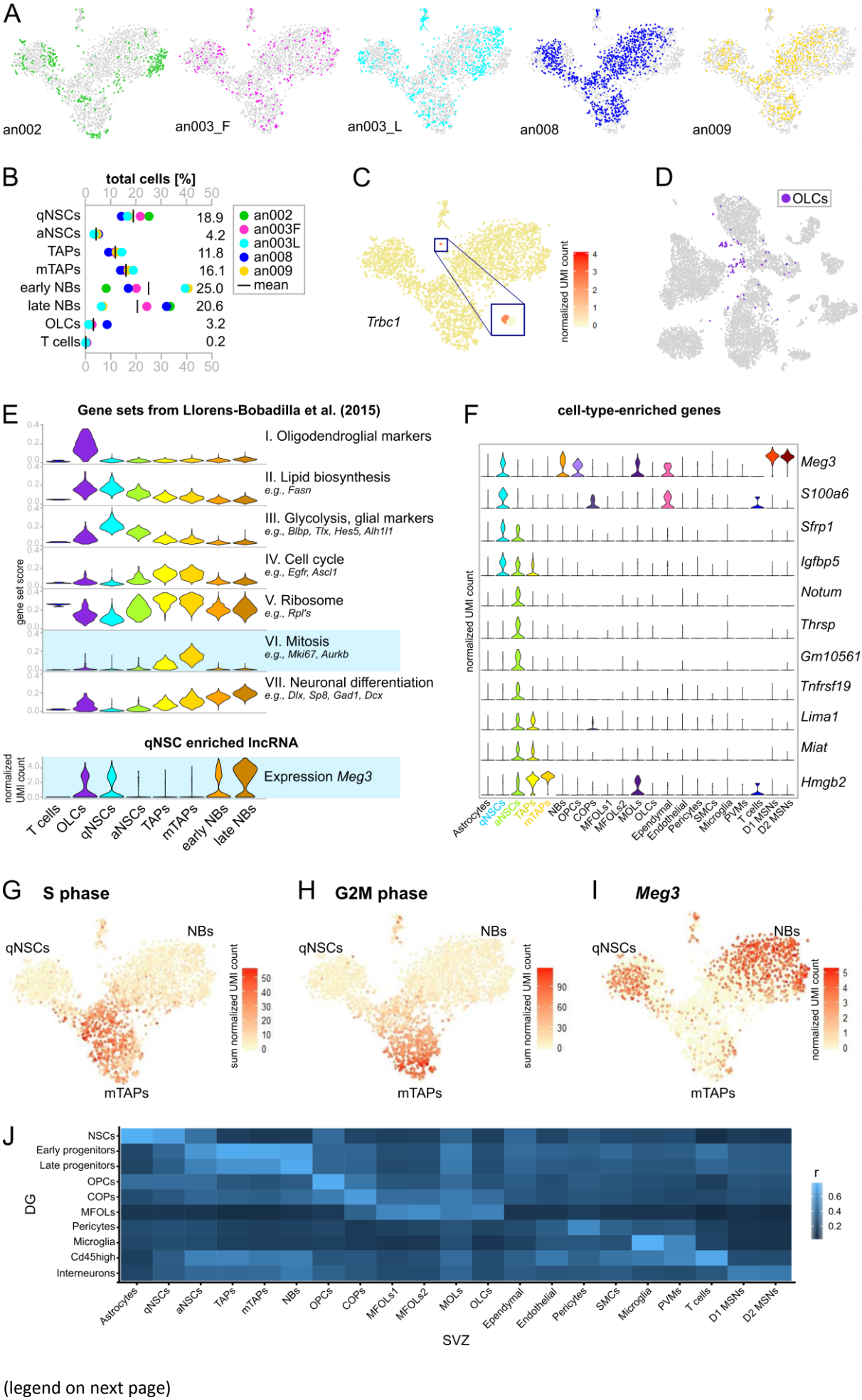

(legend on next page)

Figure S4. Subcluster characterization, NSC activation-state enriched genes, and comparison with DG. Related to Figures 2 and 3.

(A) Distribution of replicates in the tSNE plot of the subclustering. Cells from one replicate are colored and plotted on top of all other cells (in gray).

(B) Proportions of cell types after subclustering. Numbers represent the mean.

(C) tSNE plot of the subclustering colored by the expression of T cell receptor *Trbc1*. The expression of T cell receptors was specific for subcluster 1 (blue square represents a close up) disclosing these cells as contaminating T cells. Of note, the subcluster consists of four cells deriving from four different replicates.

(D) Localization of oligodendrocyte-like cells (OLCs, in purple) in the all-cell tSNE plot. In the subclustering analysis, subcluster 2 separated due to oligodendrocyte associated genes (gene set I, panel E). However, OLCs also expressed some glial and neuroblast genes (gene sets II, III and VII, panel E) and localized close to NSCs, TAPs, and NBs in the all-cell tSNE plot (panel D) suggesting that OLCs might represent cell doublets. As two previous single-cell RNA sequencing studies also observed OLCs within their FACS-sorted populations (Dulken et al., 2017; Llorens-Bobadilla et al., 2015) we doubt that these cells are doublets, but hypothesize that they might represent a so far uncharacterized cell type.

(E) Characterization of subclusters based on gene sets published in Llorens-Bobadilla et al. (2015). At the bottom: the expression of the long non-coding RNA (lncRNA) *Meg3* negatively correlates with the expression of mitotic genes (blue background). See also panels G-I.

(F) NSC activation-state enriched genes in the context of all identified cell types from Figures 2A and 3C.

(G, H) Expression sum of S (G) and G2M (H) phase associated genes (from Tirosh et al., 2016) in the tSNE plot of the subclustering.

(I) Expression of the lncRNA *Meg3* in the tSNE plot of the subclustering.

(J) Gene expression profiles of SVZ and DG cell types correlate well. The heatmap depicts Pearson correlation (r, bright indicates high, dark indicates low correlation). Cell types on the y axis (DG) were characterized in Artegiani et al. (2017).

Cell type abbreviations as in Figures 2 and 3.

A

exp_ID	genotype	fixation	sex	# animals	age (weeks)	# cells	median UMIs/cell	median genes/cell
an007_WT	wildtype and heterozygous	-	m	4	11.3	2604	943	660
an010_WT	littermate controls (Ctr)	-	m	4	11.4	1713	1118	725
an007_KO	LRP2-deficient (KO)	-	m	3	11.3	2698	940	668
an010_KO		-	m	4	11.4	1041	1166	754

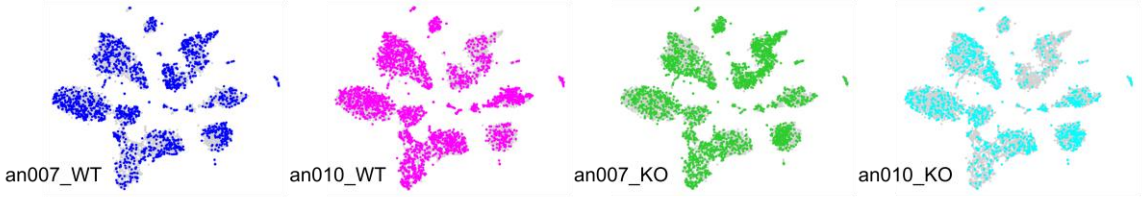

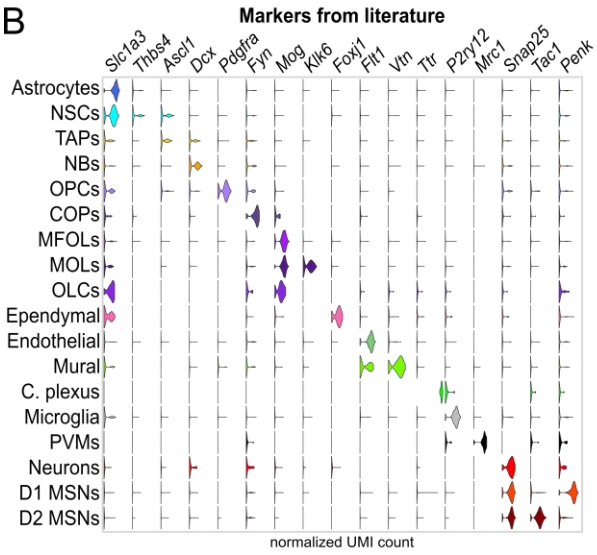

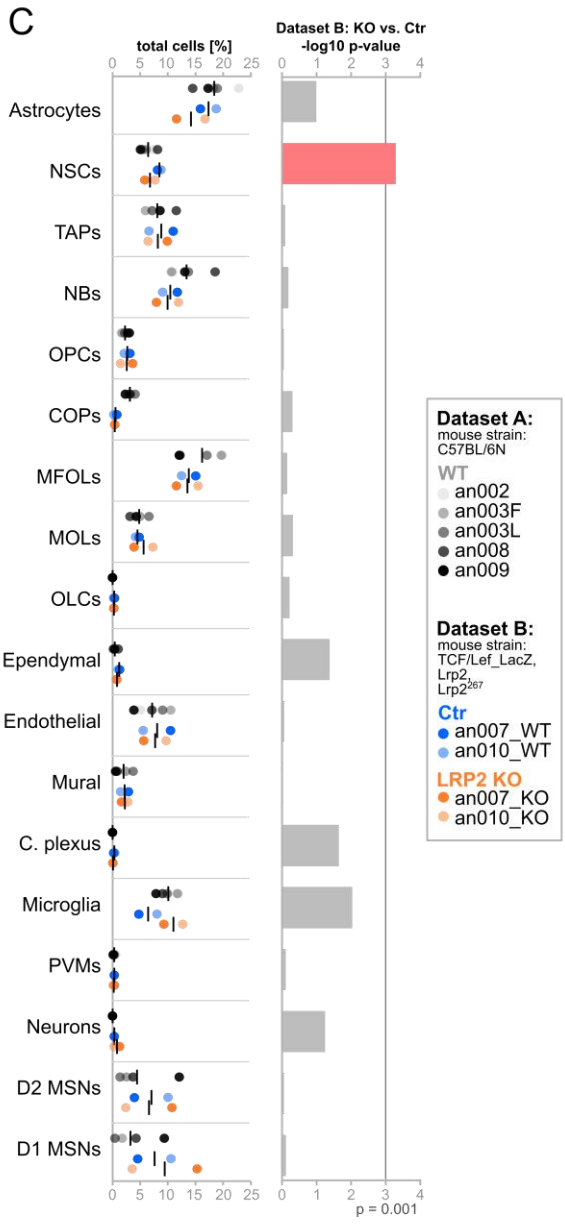

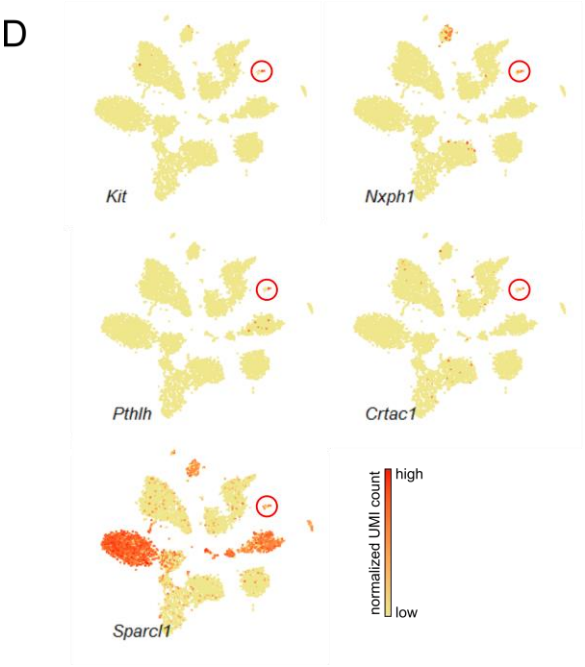

Figure S5. Cluster composition, cell type identification and distribution of replicates across cell types in the LRP2 KO/Ctr Drop-seq analysis (dataset B). Related to Figure 4. (legend on next page)

Figure S5. Cluster composition, cell type identification and distribution of replicates across cell types in the LRP2 KO/Ctr Drop-seq analysis (dataset B). Related to Figure 4.

(A) Overview of replicates and distribution of replicates in the all-cell tSNE plot. Cells from one replicate are colored and plotted on top of all other cells (in gray). an007_WT contained cells derived from one wild-type and three heterozygous mice. For an010_WT, two wild-type and two heterozygous mice were used.

(B) Identification of cell types based on known marker genes.

(C) Proportions of cell types in dataset A (gray, wild-type) and dataset B (blue, control; orange, LRP2-deficient mice). Right panel: P-values from the comparison of cell type proportions in dataset B: Ctr vs. KO. Statistical significance of data was determined using a generalized linear mixed model. The p-value for NSCs is highlighted in red.

Abbreviations: exp_ID: experiment identifier; m = male; KO: LRP2-deficient mice, Ctr: wild-type and heterozygous littermate controls; C. plexus: choroid plexus, OLCs: oligodendrocyte-like cells, other cell type abbreviations as in Figure 2.

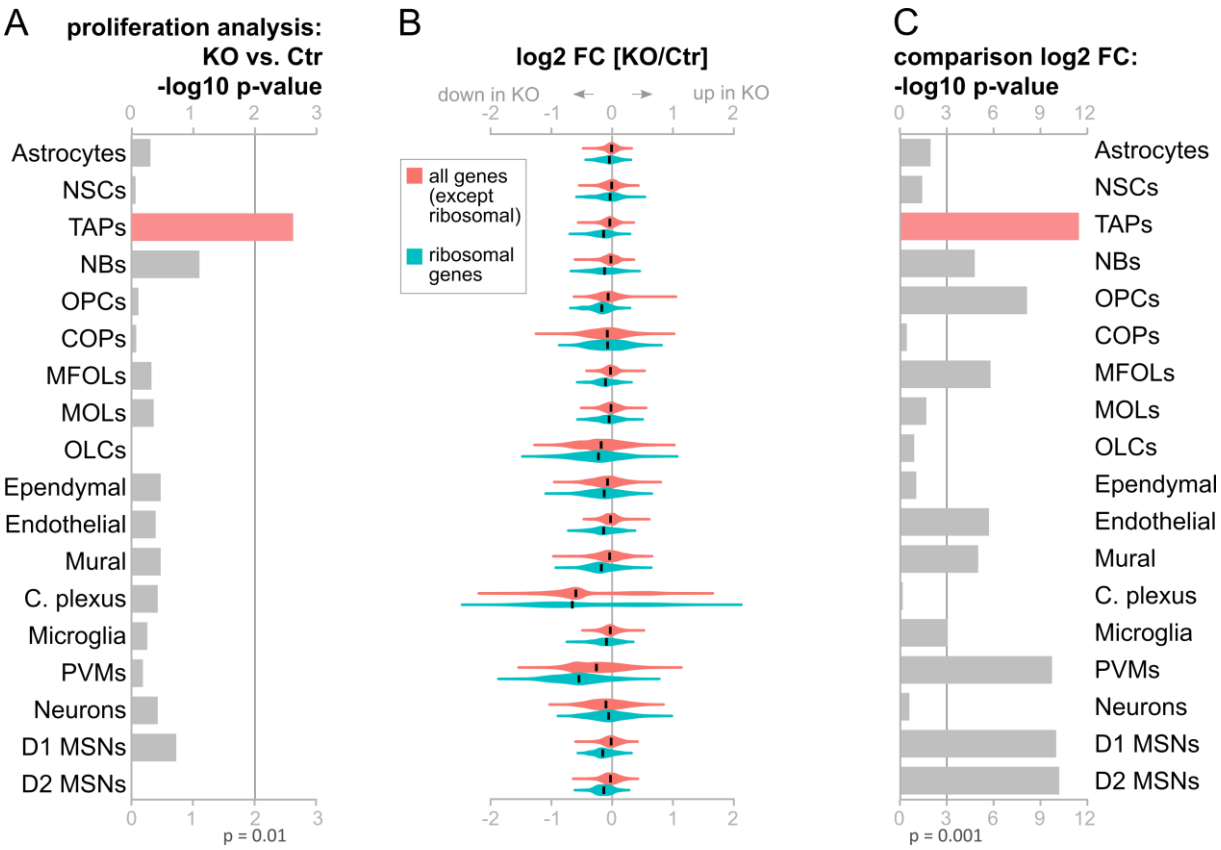

Figure S6. Proliferation is significantly reduced in TAPs, and ribosomal genes are decreased in the LRP2-deficient SVZ. Relate to Figures 4 and 5.

(A) P-values of the proliferation analysis for all cell types. Statistical significance of data was determined using Kolmogorov-Smirnov test between the cumulative fraction distributions of cells scored for cell cycle (LRP2 KO versus Ctr). The p-value for TAPs is highlighted in red.

(B) Distribution of log2 fold changes (LRP2 KO versus Ctr, cells averaged per cluster) of ribosomal (teal) and all remaining genes (red). Expression cut off ≥ 0.5 log2 (mean normalized UMI count) Ctr cells.

(C) P-values for panel (B). In 10 of 18 identified cell clusters, ribosomal genes were significantly lower expressed as all remaining genes in cells derived from LRP2 KO compared to Ctr SVZ (p-value < 0.001). TAPs (highlighted in red) had the smallest p-value. Statistical significance of data was determined using unpaired Student's t test.

Abbreviations: FC: fold change; all other abbreviations as in Figure S6.